International Journal for Numerical and Analytical Methods in Geomechanics

WILEY

RESEARCH ARTICLE OPEN ACCESS

Laboratory-Scale Free Fall Cone Penetrometer Test on Marine Clay: A Numerical Investigation Using the Generalized Interpolation Material Point Method

Debasis Mohapatra[1] | Saeideh Mohammadi[1] | Maarit Saresma[2] | Joonas J. Virtasalo[2] | Wojciech T. Sołowski[1]

[1]Department of Civil Engineering, Aalto University, Espoo, Finland | [2]Geological Survey of Finland (GTK), Espoo, Finland

Correspondence: Debasis Mohapatra (debasis.mohapatra@aalto.fi)

Received: 8 April 2024 | **Revised:** 30 October 2024 | **Accepted:** 16 December 2024

Funding: This project has received funding from the European Union—NextGenerationEU instrument and is funded by the Research Council of Finland under grant number 347602. This study has utilized research infrastructure facilities provided by the Finnish Marine Research Infrastructure (FINMARI) network.

Keywords: clay destructuration | digital image processing | dynamic penetration | free fall cone penetrometer test | generalized interpolation material point method | strain rate effects

ABSTRACT

This paper presents a series of laboratory free-fall cone penetrometer (FFCP) tests conducted on marine clay samples collected from the Gulf of Finland in the Baltic Sea. Subsequently, these tests are replicated numerically with the generalized interpolation material point method (GIMP) simulations. First, the paper gives laboratory-scale FFCP experiment results used for the validation of the numerical framework. In these experiments, a small-scale model of a FFCP was dropped from various heights into a natural marine clay soil sample and recorded using a high-speed camera. The tests were supplemented with a laboratory test program to determine the geotechnical properties of the clay used in the experiments. Following image processing, the tests provided data for numerical simulations: displacement, velocity, acceleration, and reaction force curves associated with the FFCP during the penetration process. The GIMP simulations shown in the paper replicate the process of penetration of the FFCP into the marine clay. The simulations used a strain-rate dependent Tresca constitutive model, extended with strain softening that replicates the reduction of the undrained shear strength due to destructuration, an important feature of the material. The numerical simulations replicate the experiments well. The study examines the effect of cone penetrometer roughness, impact velocity, mesh density, strain rate, and strain softening on the cone penetrometer penetration process. The simulation results indicate that the presented framework can replicate the dynamic penetration process on soft and sensitive clay very well.

1 | Introduction

The characterization of seabed surface layer strength is crucial for the design of pipelines, flow lines, and anchors. The seabed surface sediments are often very soft and sensitive. Due to their characteristics and location, obtaining high-quality soil samples for tests in the laboratory is challenging. In situ testing, such as a free fall cone penetrometer test (FFCPT) [1] is an alternative to laboratory tests. In FFCPT, a free fall cone penetrometer (FFCP) is dropped from a ship falling freely until impacting the seabed and penetrating a few meters of deposits. The FFCPT interprets the undrained shear strength (s_u) profile of the seabed clay layer based on the dynamic penetration resistance offered by the soil during the penetration process [1–5].

The FFCPT is a simple, rapid, and cost-effective test [4]. However, despite successful applications, there are still uncertainties in the interpretation of the test data and its correlation with the soil properties. The currently used correlations are empirical, analytical, and semi-analytical, mainly because of the complexities associated with the numerical simulation of the dynamic penetration process [6–10]. Therefore, developing reliable numerical models that can replicate the dynamic penetration process may lead to more accurate correlations and data interpretation, improving the accuracy of the soil properties obtained with FFCPT.

In recent years, numerous investigations have been conducted to interpret soil properties from FFCPT data, employing semi-empirical [11–14], semi-analytical [1, 15–18], and numerical methods [7, 9, 10, 19, 20]. These studies have underscored that uncertainties in interpreting FFCPT data can arise from the wide range of strain rates encountered during testing [8–11, 17, 21]. Cross-examining the FFCPT data against, for example, laboratory tests is problematic, as obtaining high-quality samples from offshore is challenging, time-consuming, and expensive.

The resistance of soils in FFCPT is notably higher compared to conventional cone penetration tests (CPT) [11, 17, 22]. This increase is mainly due to the rapid penetration rate in FFCPT, which generates a high shear strain rate, resulting in greater shear strength. The rise in shear strength with strain rate occurs mainly because of inertial effects, changes in pore pressure, and structural rearrangements within the soil [22]. Determining the strain rate effect on the shear strength of soil is complex due to its potential dependency on various factors, including soil properties (e.g., strength, stress history), cone penetrometer parameters (e.g., geometry, density), and impact velocity. Furthermore, marine clays are often sensitive, and their undrained shear strength reduces during the cone penetration process due to the destructuration of clay [23, 24]. The recent studies by the authors show that neglecting the effects of strain rate and destructuration of clay significantly influences the accuracy of numerical simulation of the dynamic penetration process [25].

The main objective of this study is to enhance the experimental and numerical understanding of the FFCP penetration process into soft and sensitive marine clay. Additionally, the research aims to provide well-controlled laboratory test data that can be used to validate numerical models (refer to Appendix A). These tests were supplemented with a laboratory test program designed to determine the geotechnical properties of the soil utilized in the experiments. The displacement, velocity, and acceleration profiles associated with the FFCP penetration process of the FFCPT experiments are obtained by image processing techniques.

The study proposes a numerical framework capable of simulating the FFCPT in marine clays. The numerical simulations use GIMP combined with an extended Tresca material model to consider the effect of strain rate and destructuration of clay to model the free fall cone experiments on soft and sensitive marine clay. The analysis employs a friction contact algorithm to model the interaction between clay and FFCP. The numerical simulation results that consider the effect of strain rate and destructuration of clay are in good agreement with the experimental observations.

The novelty of the paper lies in obtaining high-quality experimental data and replicating it with sophisticated numerical simulations to provide comprehensive insights into the penetration mechanisms of the FFCP in soft and sensitive marine clay. Presented research investigates cases where the FFCP impacts the soil surface with an initial velocity, unlike in more traditional fall cone tests (FCTs). This approach provides a more realistic representation of field conditions and soil responses. To achieve that we:

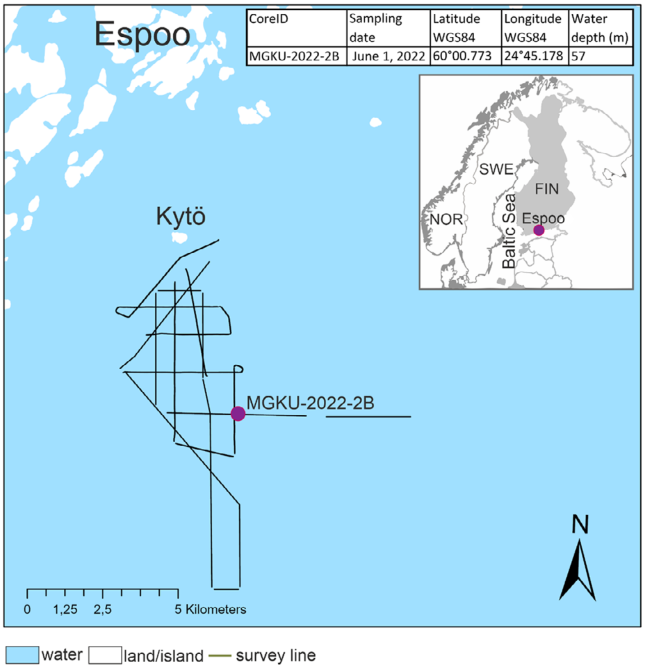

FIGURE 1 | Location of the study area in the neighborhood of Kytö island, in the Gulf of Finland. Map Copyright National Land Survey of Finland.

- created an amended FFCP laboratory setup that allows for tailored image processing techniques and other algorithms enhancing the accuracy of the image processing, leading to obtaining accurate displacement, velocity, and acceleration profiles associated with the laboratory FFCPT
- tested marine clay samples from Finnish coastal areas
- obtained high-quality data from the experiments, useful, for example, for validating future numerical models
- introduced and validated a numerical framework capable of simulating FFCPT in marine clay considering factors such as strain rate and clay destructuration. This framework offers a more realistic representation of soil response during penetration.

2 | Experimental Methods

2.1 | Soil Samples

The study uses offshore clay samples collected from the seabed near Kytö island in the Gulf of Finland, north of the Baltic Sea (Figure 1). The study area is in the outer part of a coastal archipelago with shallow water (water depth ≈ 57 m). The salinity of seawater at the study site is approximately six parts per thousand (ppt), which is much lower than the typical salinity of marine clay, usually around 35 ppt. Therefore, the clay found at

TABLE 1 | Summary of soil properties obtained from soil testing program.

Parameter	Value
Depth (m)	2.6–3.4
Density, ρ (g/cm$^{3)}$	1.4 ± 0.1
Water content, W (%)	130 ± 5
Sensitivity, s_t	10 ± 2
Particle density, ρ_s (g/cm^3)	2.72 ± 0.03
Organic content (%)	5 ± 0.5

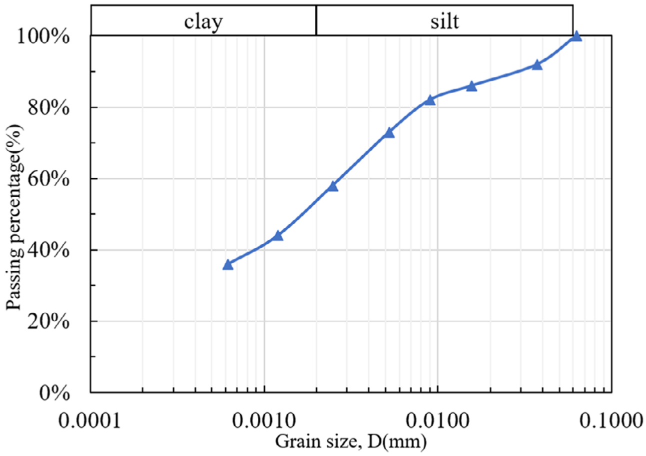

FIGURE 2 | Grain size distribution curve of Kytö clay.

the site could be classified as backwater or brackish water clay [26]. The brackish water clay at the site is underlain by postglacial lacustrine silty clay [27, 28]. However, in this paper, we will refer to it simply as marine clay. The soil cores up to a depth of 4.5 m were collected from the site with the help of 58 mm diameter PVC tubes by using the piston coring technique. Three collected soil cores (MGKU-2022-1B, MGKU-2022-2B, and MGKU-2022-3B) from the site were transported to the geotechnical laboratory of Aalto University for laboratory studies. The soil samples were stored in a cold room at 6°C until used in the experiment. The laboratory testing program involved establishing the water content, sensitivity, organic content, and grain size distribution. Then, based on triaxial tests, we directly estimated the undrained shear strength (s_u) of clay. The experimental data presented here are based on tests carried out on a soil section collected from a depth of 2.7–3.2 m of the soil core MGKU-2022-2B, see Table 1. Figure 2 shows the grain size distribution curve of the Kytö clay. The sample is classified as silty clay with 57% clay content and 42% silt content (European Standard EN ISO 14688-2). As confirmed by oedometric tests, Kytö clay is normally consolidated, which is typical for recently deposited marine clays. For more information on the soil properties of Kytö clay, please see Appendix B.

2.2 | Undrained Shear Strength

The aim is to obtain the undrained shear strength as accurately as possible, based on triaxial tests. The triaxial specimens of 100 mm height and 50 mm diameter were prepared following the guidelines of the European Standard EN ISO 17892–9:2018. The triaxial test is conducted on a soil section ranging from 2.77 to 2.87 m to directly ascertain a representative value of the undrained shear strength (s_u) for the soil core depth utilized in the current analysis (2.7–3.2 m). Since the samples may have been disturbed during collection and the stress state might not be well preserved in the PVC tubes, the first step of the test was to anisotropically consolidate the samples, recreating the in situ stress with 11.6 kPa vertical and 7.0 kPa horizontal stress. After consolidation, the specimens were sheared in undrained condition, with a strain rate of 0.6% per hour until a specified failure criterion occurred or until a strain of 15% was reached. Figure 3 shows the stress–strain curve in terms of deviator stress $q(=\sigma_a-\sigma_r)$ against the axial strain ε_a. The parameters σ_a and σ_r represent the total axial stress and total radial stress, respectively. The value of undrained shear strength (s_u) is defined as half the maximum q before or when axial strain reaches 15%. This leads to the calculated value of undrained shear strength 6.7 kPa.

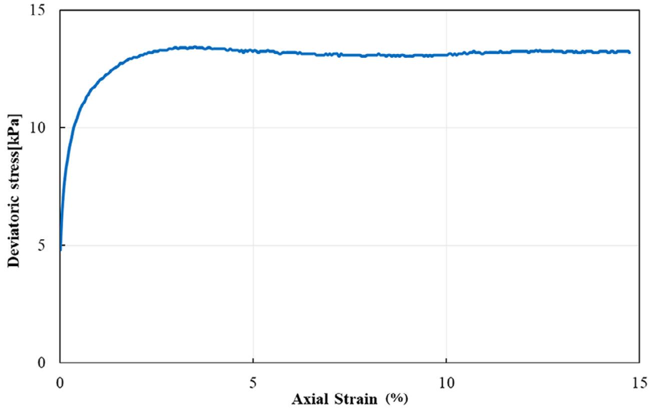

FIGURE 3 | Undrained triaxial test result, deviator stress against axial strain plot.

TABLE 2 | The undrained shear strength (s_u) values obtained from the triaxial test at different depths of the soil core.

Depth of soil core (m)	s_u from triaxial test (kPa)
1.5–2.6	6.7
2.77–2.87	**6.7**
3.77–3.87	6.8

Bold represents important values.

To attain a more accurate measurement of the undrained shear strength of the soil layer, triaxial tests are conducted on soil samples from above (1.6–2.6 m) and below (3.77–3.87 m) the current soil layer in a similar manner. Table 2 shows the undrained shear strength (s_u) values obtained from the triaxial test conducted at different depths (1.5–3.9 m) of the soil core. The undrained shear strength value of clay does not change significantly along the depth and lies between 6.7 and 6.8 kPa. Therefore, the choice of undrained shear strength value (6.7 kPa) is reasonable to be used in the present analysis. The constant rate of strain (CRS) oedometer tests were done to determine the pre-consolidation pressure, over-consolidation ratio (OCR), and compressibility parameters of undisturbed samples. The results of these oedometer tests are detailed in Appendix B.

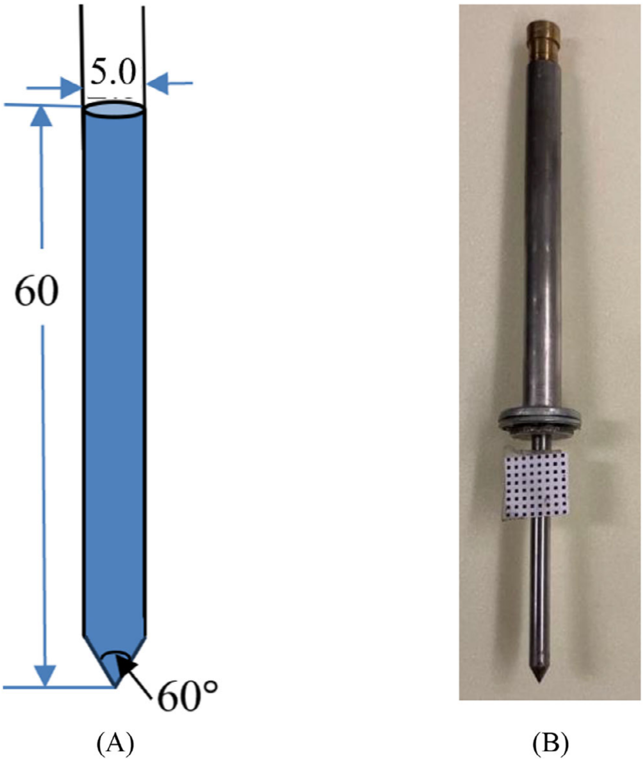

FIGURE 4 | Model free fall cone penetrometer. Unit: mm.

2.3 | Model FFCP

To understand the dynamic cone penetration mechanism associated with the FFCPT, a series of well-controlled laboratory scale model tests were conducted using a laboratory scale FFCP. The model tests were conducted using an in-house fabricated cone penetrometer under controlled conditions. The model FFCP, shown in Figure 4B, has a similar geometry to the Graviprobe 2.0 (dotOcean), which is often used in in-situ FFCPT. The FFCP is a steel cone of 5 mm diameter and 60 mm length with a 60° apex angle (Figure 4A). Some additional steel weights were attached at the bottom of the shaft to increase its weight to 60 g (see Figure 4B). The steel shaft was attached to a frame, from which it could be released from different heights into the soil sample to generate different impact velocities. The dial gauge was attached to the frame to measure the final penetration depth (see Figure 5). The conventional FCT were also carried out by using a 30°, 100 g cone and a 60°, 60 g cone.

2.4 | Laboratory Scale FFCPT Procedure

To understand the dynamics of the FFCP penetration and gather data to be later replicated by numerical simulations, we made a series of well-controlled free fall cone penetration experiments. The clay specimens for the FCTs were approximately 50 mm thick and were extruded from the sampling tube and then cut with a wire saw. The penetration tests were performed at five different points on each soil specimen. The first impact point was positioned at the center of the sample, while the other four were symmetrically distributed across the sample surface, approximately midway between the center and the sample perimeter. This setup ensured a consistent spacing of about 14 mm between each point and the sample boundary. Numerical analysis from Section 4.2 revealed that soil disturbance is mostly confined within 10 mm of the center of the FFCP. Additionally, a statistical study referenced in [29] found no significant difference in undrained shear strength between tests conducted at the sides and those in the middle of the sample. Therefore, each selected point in this test was believed to be sufficiently distant from previous penetration tests to avoid any influence from prior disturbances or the sample boundary.

2.5 | Digital Image Processing of FFCPT Movie Frames

The FFCP penetration process was recorded with a high-speed camera (1000 frames/s) and tracked based on image analysis using a large number of trackable featured points. The present study uses the minimum Eigenvalue algorithm developed by [30] to detect and Kanade–Lucas–Tomasi (KLT) algorithm [30, 31] to track the featured points. The tracked points are a grid of black tracking markers on a white paper featuring attached to the model FFCP, as shown in Figure 5. The camera is placed at the front of the FFCPT apparatus with light and background colors chosen to avoid reflections and reduce noise (see Figure 5). The tracked points produce the displacement–time profiles in image space coordinates (pixels). Using an appropriate scaling factor, the displacement–time profiles produced from the image analysis in image space coordinates (pixels) are transformed into object space coordinates (meters). The velocity–time profiles associated with the tracking points are obtained by numerically differentiating the displacement–time profiles using the central difference method, while the acceleration curve is obtained by numerically differentiating the velocity curve.

For the differentiation, the velocity curve needs to be sufficiently smooth. The numerical differentiation of the displacement leads to a noisy curve, likely due to the error associated with the individual points displacement estimation. The smoothed velocity curve is obtained by taking the average velocity of all the tracking points. In the cases where the velocity curve is still not smooth enough to obtain acceleration of the FFCP, a low pass filter is used to remove the noise.

The reaction force on the FFCP, which represents the dynamic soil resistance during the penetration process, can be used to estimate the undrained shear strength (s_u) of the clay. By measuring the acceleration of the FFCP using digital image processing techniques, the reaction force on the FFCP can be estimated based on Newton's second law of motion:

$$Q = W - ma \tag{1}$$

where Q is the reaction force on the FFCP, W is the weight of the FFCP, m is the mass of FFCP, and a is the acceleration of FFCP. The reaction force on the FFCP is dynamic and depends on several factors such as impact velocity (V_i), friction between the whole FFCP tool and soil, and the strain-softening of clay during the penetration process.

Refer to the MATLAB script 'Track_FFCP.m' in the Supporting Information, which is used to obtain the displacement, velocity, acceleration, and reaction force of the FFCP during the FFCP

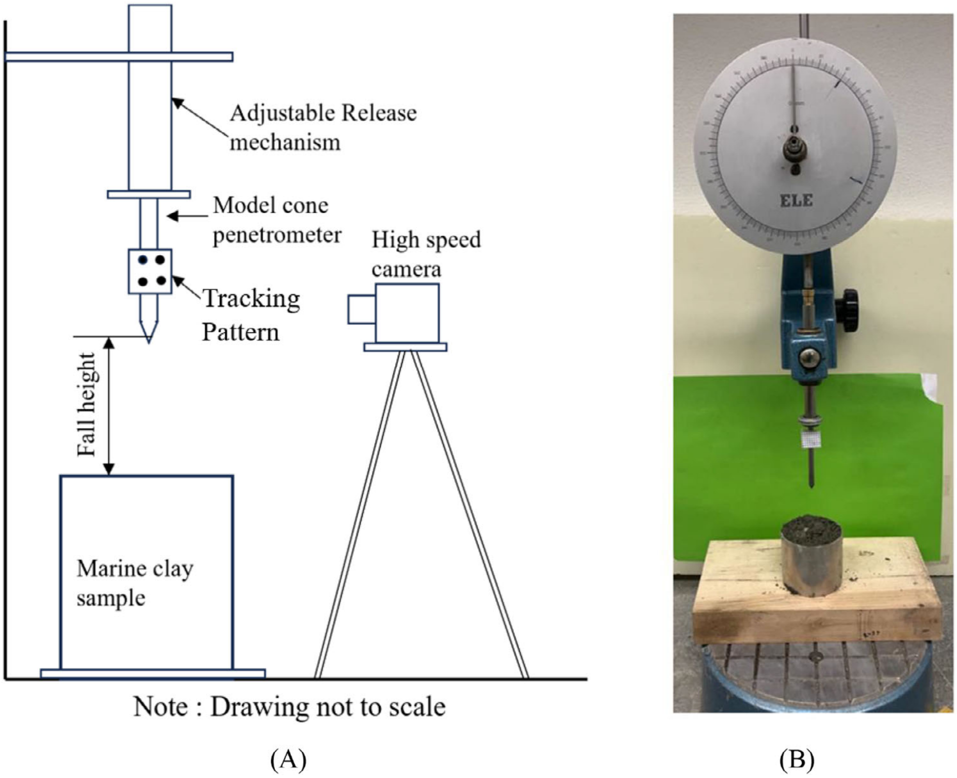

FIGURE 5 | Laboratory-scale free fall cone penetrometer test set up.

TABLE 3 | Final penetration depth of cone (D_f) from different fall cone experiments.

30°, 100 g cone		60°, 60 g cone	
Test ID	**Final penetration depth (D_f, mm)**	**Test ID**	**Final penetration depth (D_f, mm)**
E-30-1	11.1	E-60-1	4.6
E-30-2	11.6	E-60-2	4.6
E-30-3	12.4	E-60-3	4.2
E-30-4	11.6	E-60-4	4.5
E-30-5	11.5	E-60-5	5.0
Average	**11.64**	**Average**	**4.58**
Numerical model	**11.93**	**Numerical model**	**4.5**
Difference (%)	**2.5**	**Difference (%)**	**1.75**

Bold represents important values.

penetration process. More details about the validation of the combined high-speed photogrammetry and digital image processing technique can be found in [25, 32].

2.6 | Test Program

The present test program involves five test series, including 10 laboratory FCTs and 15 laboratory-scale FFCPT. Table 3 shows the list of FCTs presented in this paper. The first group of fall cone experiments was conducted by using a 30°, 100 g cone with a drop height, $D_h = 0$ (E-30-0-1 to E-30-0-5). The second group of experiments was conducted by using a 60°, 60 g cone with $D_h = 0$ (E-60-0-1 to E-60-0-5). Table 4 shows the list of model FFCPTs presented in this paper. The group of experiments was conducted by using a FFCP with a drop height, $D_h = 0$ (E-CP0-1 to E-CP0-5), $D_h = 10$ mm (E-CP1-1 to E-CP1-5), and $D_h = 20$ mm (E-CP2-1 to E-CP2-5). The values of final penetration depths (D_f) associated with different sets of experiments and their representative average values are reported in Tables 3 and 4. Detailed experimental data can be found in Appendix A.

2.7 | Experimental Investigation of FFCP Penetration Mechanism

MATLAB script 'Track_FFCP.m' (refer to Supporting Information) utilizes an image processing technique described in Section 2.5 to analyze data and generate displacement, velocity, acceleration, and reaction force profiles for the experiments

TABLE 4 | Experimental data from different free fall cone penetrometer tests (FFCPT).

Drop height	**Test ID**	**Final penetration depth (D_f, mm)**	**Peak velocity (V_p, m/s)**	**Maximum deceleration (D_{max}, m/s^2)**	**Maximum reaction force (Q_{max}, N)**
$D_h = 0$ mm	E-CP0-1	5.5	0.185	10.18	1.20
	E-CP0-2	5.5	0.184	9.47	1.16
	E-CP0-3	5.4	0.181	9.13	1.14
	E-CP0-4	5.3	0.182	11.37	1.27
	E-CP0-5	4.8	0.167	10.59	1.22
	Average	**5.3**	**0.18**	**10.15**	**1.20**
	Numerical Model	**4.9**	**0.181**	**11.00**	**1.25**
	Difference (%)	**8.2**	**5.6**	**8.37**	**4.17**
$D_h = 10$ mm	E-CP1-1	11.1	0.472	17.9	1.66
	E-CP1-2	10.1	0.46	18.45	1.70
	E-CP1-3	11.6	0.47	16.41	1.57
	E-CP1-4	11.0	0.45	16.10	1.55
	E-CP1-5	10.6	0.434	16.5	1.58
	Average	**10.8**	**0.457**	**17.07**	**1.61**
	Numerical Model	**10.4**	**0.46**	**16.51**	**1.58**
	Difference (%)	**3.7**	**0.65**	**3.28**	**1.86**
$D_h = 20$ mm	E-CP2-1	12.7	0.573	19.74	1.77
	E-CP2-2	13.6	0.64	23.98	2.03
	E-CP2-3	12.4	0.62	25.37	2.11
	E-CP2-4	13.3	0.64	23.72	2.01
	E-CP2-5	12.3	0.62	23.24	1.98
	Average	**12.85**	**0.619**	**23.21**	**1.98**
	Numerical model	**13.8**	**0.644**	**19.44**	**1.76**
	Difference (%)	**7.4**	**4.0**	**16.24**	**12.5**

Bold represents important values.

discussed in Section 2.6. Figure 6A,B show the displacement profiles associated with different experiments conducted using 30° 100 g and 60° 60 g cones when the cone is released from the surface of the soil specimen ($D_h = 0$). Figures 7–9 give the displacement, velocity, acceleration, and reaction force profiles associated with the FFCPT, when the FFCP is dropped from a drop height of 0, 10, and 20 mm from the soil surface, respectively. The FFCP experiments carried out at different points on the same soil sample have similar displacement, velocity, acceleration, and reaction force profiles. The acceleration profiles in Figure 7C show that the acceleration at the very beginning of the experiment was lower than the gravitational acceleration, as it takes the FFCP 0.01–0.02 s to reach the free-fall condition. This slowdown may be caused by the equipment used, specifically by the friction mobilized in the FFCP shaft during the FFCP release. This was also observed in FCTs done with similar equipment, see Mohapatra et al. [25].

The examination of Figures 8 and 9 reveals that the FFCP takes approximately 0.01–0.02 s to reach the free-fall condition. Then the FFCP moves with gravitational acceleration until it touches the soil sample surface. As soon as the FFCP touches the sample surface, the FFCP starts decelerating and finally, the acceleration becomes zero when the FFCP stops moving. There are some oscillations observed in the acceleration–time curves, these are mainly due to the approximations involved in the numerical differentiation technique we used to obtain the curves. The velocity curves in Figures 8 and 9 show that the velocity of the FFCP starts increasing as soon as it is dropped, and the velocity of the FFCP attains the peak value after it touches the sample surface when the acceleration of the FFCP is negative. The reaction force curves in Figures 8 and 9 indicate that when the FFCP falls freely, the reaction force on the FFCP is zero. Upon contact with the sample surface, the reaction force on the FFCP increases rapidly for approximately 0.004 m depth. Subsequently, the reaction force gradually increases until reaching its peak value. Once the FFCP ceases movement, the reaction force decreases to a value equal to the weight of the FFCP. The reaction force on the FFCP increases with an increase in the impact velocity of the FFCP.

In order to obtain a better comparison between the experimental profiles, we have chosen four different parameters, which

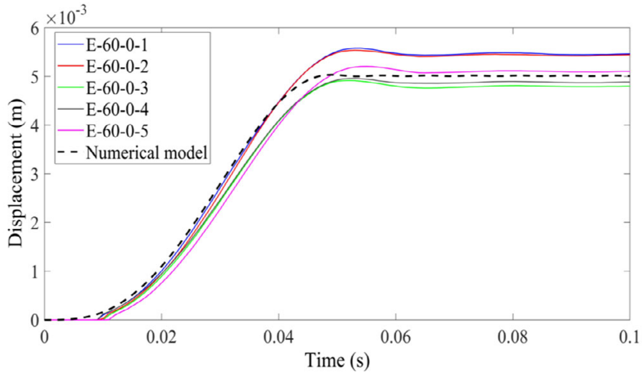

(A) 60°, 60g cone

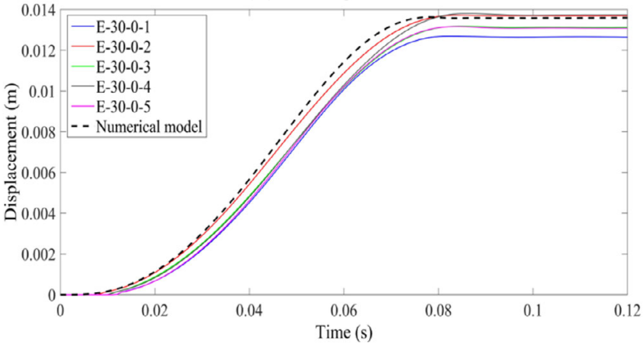

(B) 30°, 100g cone

FIGURE 6 | Displacement profiles associated with fall cone experiments.

TABLE 5 | The experimental value of time and velocity of the FFCP when it impacts the soil surface.

Drop height (D_h)	t_i (s)	V_i(m/s)
0	0	0
10 mm	0.053	0.43
20 mm	0.072	0.61

quantitatively define the curves, namely, (1) final penetration depth (D_f), (2) peak velocity (V_p), (3) maximum deceleration (D_{max}), and (4) maximum reaction force (Q_{max}). The values of these parameters associated with different FFCP experiments are reported in Table 4. The friction between the FFCP shaft and sleeve is supposed to influence the FFCP velocity during free fall and, the actual velocity of the FFCP when it hits the soil surface will be different from the theoretical value. The present experiment uses the available image processing data to calculate the impact velocity (V_i) when it touches the ground surface. For D_h= 10 mm, the impact velocity of the FFCP ranges from 0.41 to 0.46 m/s, with an average value of 0.43 m/s (refer to Appendix A). Similarly, for D_h= 20 mm, the impact velocity of the FFCP ranges from 0.57 to 0.63 m/s, with an average value of 0.61 m/s (refer to Appendix A). The experimental values of the average impact velocity and time of the FFCP upon impacting the ground surface are provided in Table 5. Additionally, the scatter in the impact velocity of the FFCP can be evaluated from Figures 8 and 9.

3 | Numerical Model

3.1 | A Brief Description on MPM Formulation

The material point method (MPM) is a numerical approach particularly well-suited for modeling history-dependent behavior in large-deformation geotechnical problems. In MPM, the calculation domain consists of Lagrangian particles embedded within a Eulerian grid [33, 34]. Each particle is characterized by its position, mass, density, velocity, deformation gradient, and any other internal state variables necessary for constitutive material models. The momentum balance equation is solved within the background grid. Material point discretization is automatically generated based on the grid structure, with the initial number of material points per element specified across the grid. Since material points, which carry all physical information, can freely move through elements, issues with mesh distortion are largely mitigated. However, particle movement in MPM can lead to numerical instabilities, such as cell crossing errors resulting from the discontinuity of the interpolation function derivative. Several methods have been proposed to address this issue [35–37]. An effective and widely accepted approach is the generalized interpolation material point method (GIMP) formulation, specifically the undeformed GIMP (uGIMP), which assumes a fixed particle size, or the convected particle GIMP (cpGIMP), which allows particles to evolve with material deformations. This paper utilizes the uGIMP algorithm as implemented in the Uintah software (http://uintah.utah.edu).

3.2 | The Material Constitutive Model for the Marine Clay

During the FCT, the cone penetrates the soil and comes to rest within 0.1 s. Therefore, for fully saturated clay, there is no water flow and hence no volume change, leading to a fully undrained behavior. This paper describes the undrained behavior of clay by an elastoplastic Tresca material model with an associated flow rule. Additionally, undrained shear strength increases with shear strain rate [24, 38, 39]. Furthermore, sensitive clay shear strength decreases with the increase in accumulated plastic strains. Therefore, in the simulations, we use the Tresca material model extended to consider the effect of strain rate and destructuration on undrained shear strength, with an exponential relation of undrained shear strength to accumulated shear strain [24, 38]. The undrained shear strength of clay is expressed as a function of strain rate ($\dot{\gamma}$), accumulated shear strain (γ), and sensitivity (s_t) as:

$$s_u\left(\dot{\gamma},\gamma,s_t\right) = s_{u,ref}\left[\left(\frac{\dot{\gamma}}{\dot{\gamma}_{ref}}\right)^{\beta}\right]\left[\frac{1}{s_t}+\left(1-\frac{1}{s_t}\right)e^{\frac{-3\gamma}{\gamma_{95}}}\right] \qquad (2)$$

where the shear strain rate ($\dot{\gamma}$) computed from the strain rate tensor:

$$\dot{\gamma} = \frac{1}{2}\sqrt{2\left(\dot{\varepsilon}_{ii}-\dot{\varepsilon}_{jj}\right)^{2}+3\dot{\varepsilon}_{ij}^{2}} \qquad (3)$$

$s_{u,ref}$ is reference undrained shear strength at reference strain rate ($\dot{\gamma}_{ref}$), β is the strain rate parameter associated with the power

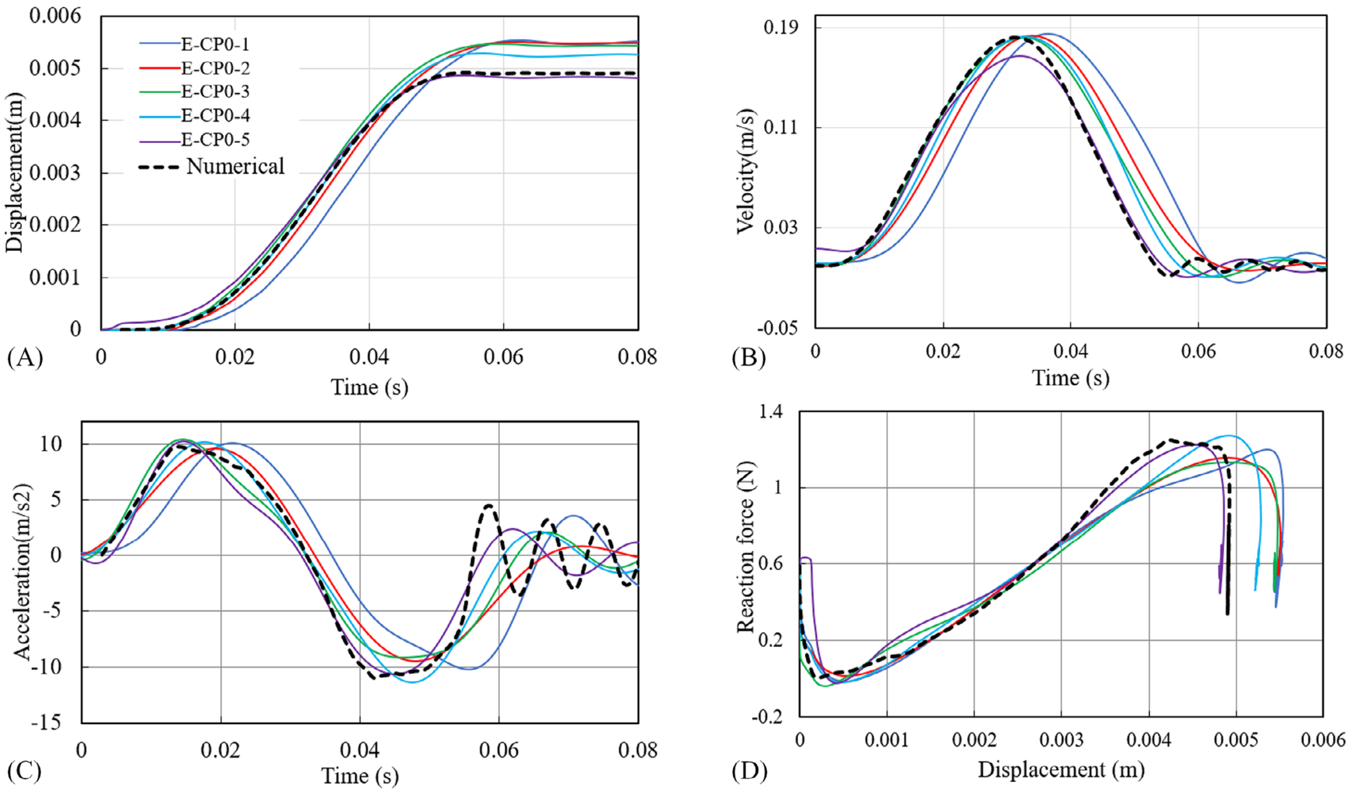

FIGURE 7 | Comparison between numerical and experimental results of the free fall cone penetrometer test (FFCPT) with drop height 0 mm.

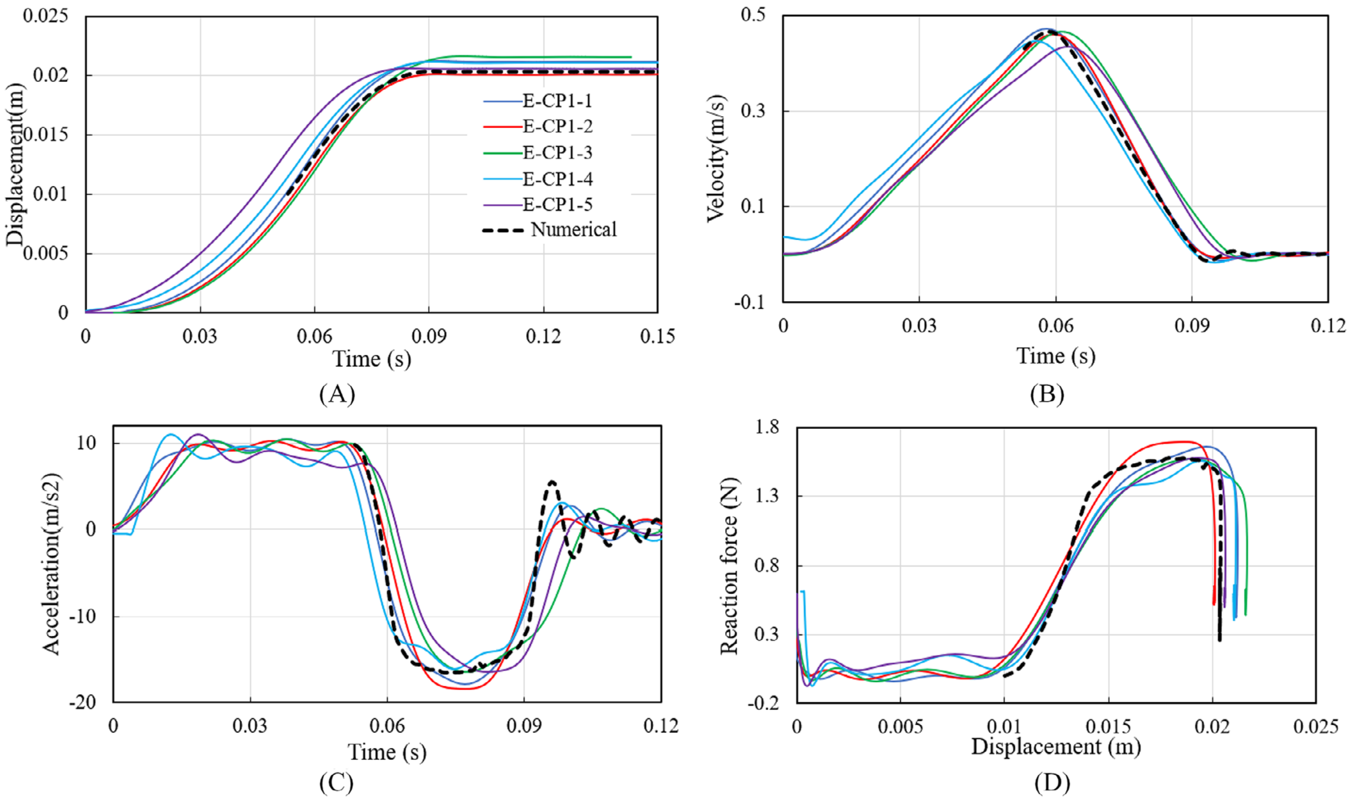

FIGURE 8 | Comparison between numerical and experimental results of the free fall cone penetrometer test (FFCPT) with drop height 10 mm.

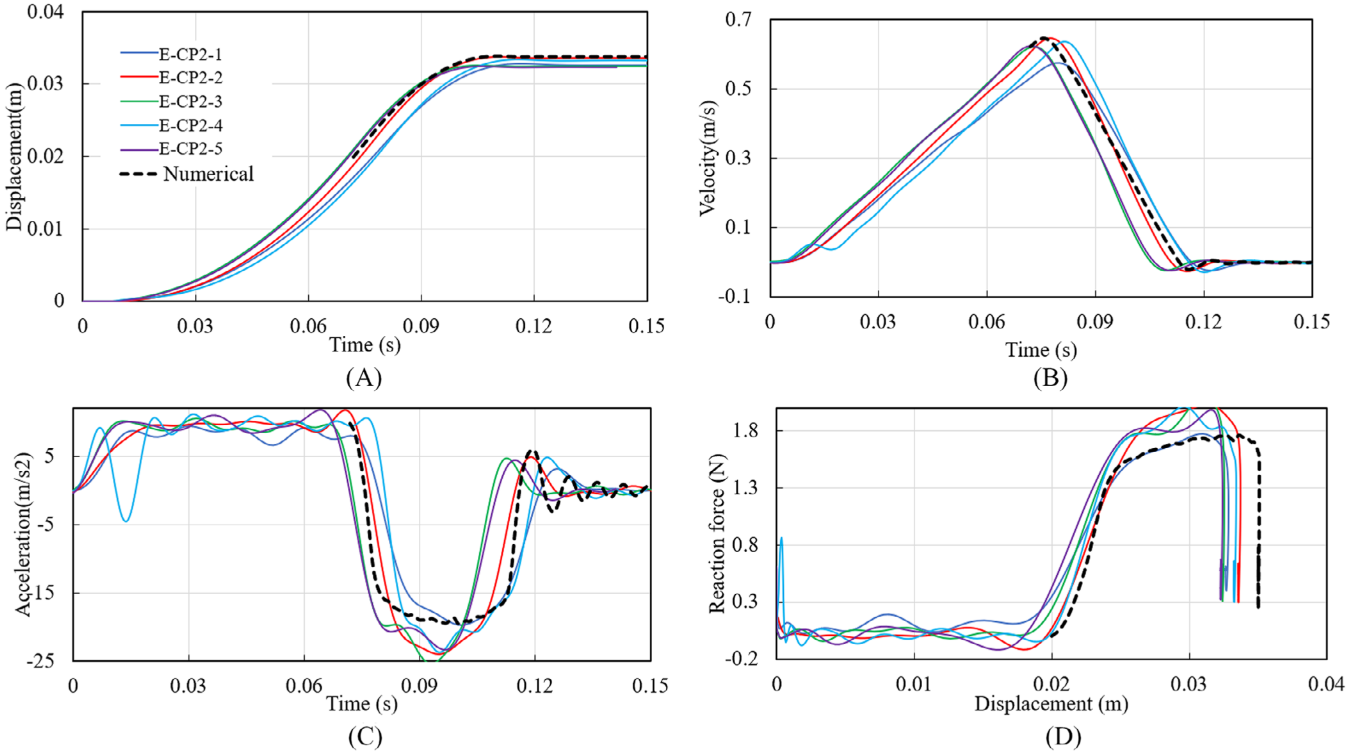

FIGURE 9 | Comparison between numerical and experimental results of the free fall cone penetrometer test (FFCPT) with drop height 20 mm.

law, and γ_{95} is the accumulated shear strains required to obtain 95% reduction of the shear strength. The first bracketed term in Equation (2) corresponds to the enhancement of undrained shear strength due to a high strain rate and, the second bracketed term represents the reduction of shear strength in line with the accumulated plastic shear strain. The multiplicative superposition principle indicated in Equation (2) is reasonably accurate [40]. For small deformations, the dynamic undrained shear modulus depends on the shear strain rate [41], therefore the dynamic undrained shear modulus can be estimated as

$$G_u\left(\dot{\gamma}\right) = G_{u,ref}\left(\frac{\dot{\gamma}}{\dot{\gamma}_{ref}}\right)^{\beta} \tag{4}$$

3.3 | Numerical Model

The GIMP simulation of the laboratory FFCPT and FCT assumes the axisymmetric condition of the fall cone experiment. Figure 10 shows the numerical model and assumed boundary conditions. The simulation assigns the axis of symmetry along the vertical axis passing through the centroid of the fall cone or the FFCP. The bottom of the soil is restrained in both the vertical and radial directions, the far boundary is restrained in the radial direction, and the top boundary remains free. The simulation uses an elastic material model for the steel penetrating devices. The height and width of the soil domain are decided based on a few trial analyses so that the bottom and side boundaries do not influence the outcome of the numerical simulation. The numerical simulation starts with the condition the FFCP tip is just touching the ground surface. The FFCP drop height (e.g., D_h= 10 mm, and 20 mm) is modelled by assigning initial velocity to the FFCP. Section 2.7 shows that the influence of friction between the FFCP and sleeve may influence the impact velocity of the cone. The present analysis uses average initial velocities (V_i) obtained from the experiments (Table 5) as the initial velocity of the FFCP to accommodate the influence of drop height.

3.4 | Selection of Material Parameters

The experimentally measured value of sensitivity (s_t) of the clay sample is approximately 10 and the density of the material is roughly 14 kN/m^3. As mentioned in Section 2, the reference undrained shear strength ($s_{u,ref}$) of clay is set to be 6.7 kPa based on the triaxial test. For the elastic part of the constitutive model, a Poisson's ratio, ν, of 0.499 (~0.5) is adopted to simulate the undrained conditions. The Young's modulus, E, of the soil is taken as 500 times the undrained shear strength, $s_{u,ref}$. Here, $s_{u,ref}$ denotes the original intact shear strength at the reference shear strain rate before softening. The reference shear strain rate ($\dot{\gamma}_{ref}$) is the strain rate below which the rate effect disappears. The range of the strain rates in FCTs is approximately 1–10 s^{-1}, which is roughly in the range of the strain rates in the vane shear tests [42]. For our numerical simulation in [25], we have used the value of the reference shear strain rate as 0.5s^{-1}. The same value of reference shear strain rate is used in the present simulation.

The simulation uses the friction contact algorithm parametrized by a friction coefficient (μ) as implemented in Uintah [43, 44], which uses logistic regression to identify the interface between two materials in contact. References [45, 46] indicate that the friction coefficient between cohesive soil and steel typically falls within the range of 0.5–0.8. To determine a reasonable value for the friction coefficient in the numerical simulation, a series of numerical studies have been conducted to assess

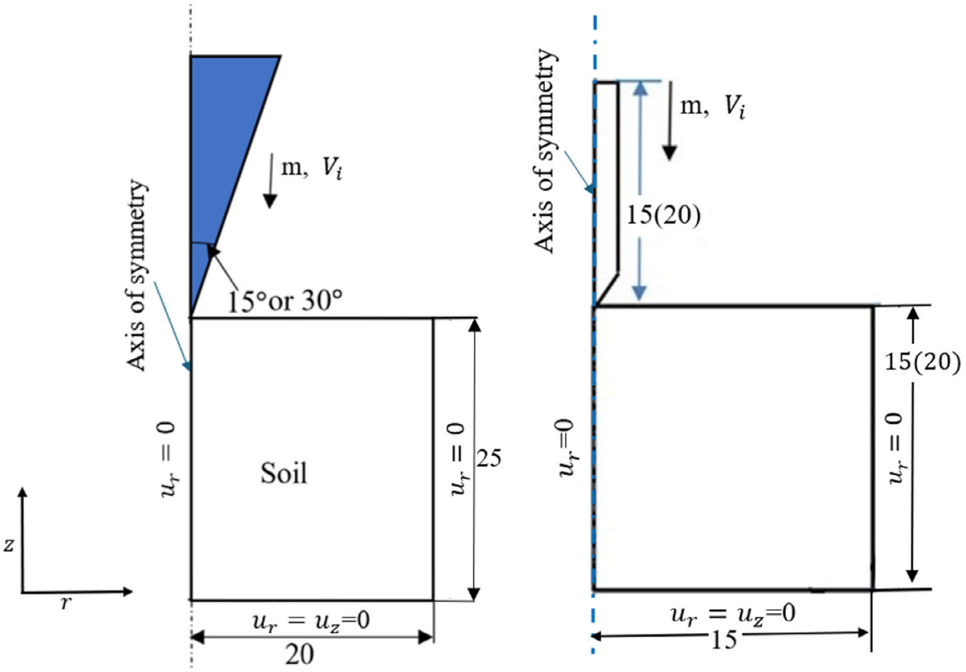

(A) Laboratory fall cone test (B) Laboratory FFCPT

FIGURE 10 | Numerical model for fall cone test (FCT) and laboratory scale FFCPT. Unit: mm. The value in parentheses represents the dimensions used for $D_h = 20$ mm.

its influence on the final penetration depth of the FFCP (D_f). This involved varying the friction coefficient (μ) from 0 to 1 for drop heights (D_h) of 0 and 20 mm. Figure 11 illustrates that friction coefficients greater than 0.7 do not significantly alter the penetration depth. Similar observations have been reported in the numerical simulation of the FCT by [23, 25, 47]. This suggests that a friction coefficient of μ= 0.7 is sufficient to prevent sliding between the cone and the soil. In this analysis, we have chosen the friction coefficient $\mu = 0.7$ to establish a rough interface between the cone and the soil. In the present study, we are not using implicit fixed contact to minimize the unwanted numerical effects related to, for examlpe, interlocking effects [48, 49] in nearly incompressible materials.

The tests are carried out on a similar type of soil (Finnish offshore clay) as that used in the experiments of Mohapatra et al. [25]. Hence, the value of β and γ_{95} are set at 0.08 and 10/s, respectively, based on our previous study on experimental and numerical simulation of the FCT [25]. To check the accuracy of the numerical model and selection of material parameters, we have numerically simulated the conventional fall cone experiments conducted by using 30° 100 g and 60° 60 g cone. The final penetration depth associated with numerical simulations is reported in Table 3. Table 3 shows that the difference between the numerical and experimental average value of the final penetration depth of the cone is less than 3% for both 30° and 60° cones. Figure 12 shows the displacement contours associated with 30° and 60° FCT at the end of the cone penetration process (refer to Appendix A for the development of displacement profiles during the cone penetration process). This validates the large deformation analysis process, selection of material parameters, constitutive model, and friction coefficient. These material parameters are further used in these simulations. Figure 7 shows a comparison between the displacement profiles associated with the fall cone experiments and numerical simulations. The profiles are matching quite well with each other.

It is well known that the inclusion of strain-softening features in standard continuum numerical methods leads to mesh-dependent strain localization problems [23, 50, 51]. To address this mesh dependency, a scaling law is applied to the numerical model by introducing an embedded shear band [23, 52]. This approach ensures that the strain energy within shear zones of thickness (t_{shear}) is consistent with the strain energy in the model with grid size (t_{model}). That leads to a scaled shear strain increment in the shear zone as

$$\dot{\varepsilon}_{scaled} = \frac{t_{model}}{t_{shear}} \dot{\varepsilon}_{model} \tag{5}$$

The shear zone thickness of the shear band is a critical parameter during failure and specifying it is required to assure convergence of the results. In this study, we assume that the shear zone thickness t_{shear} is 0.1 mm. For further details on the scaling law employed in the numerical simulation, readers are referred to [23, 50, 52]. Appendix C demonstrates that accounting for the shear band thickness significantly reduces mesh dependency.

4 | Numerical Simulation Results and Discussion

4.1 | Numerical Replication of FFCPTs With Zero Impact Velocity

The numerical analysis discretizes the problem domain depicted in Figure 10 using a structured square grid with a size $h = 0.1$ mm. A detailed mesh convergence study, along with the justification

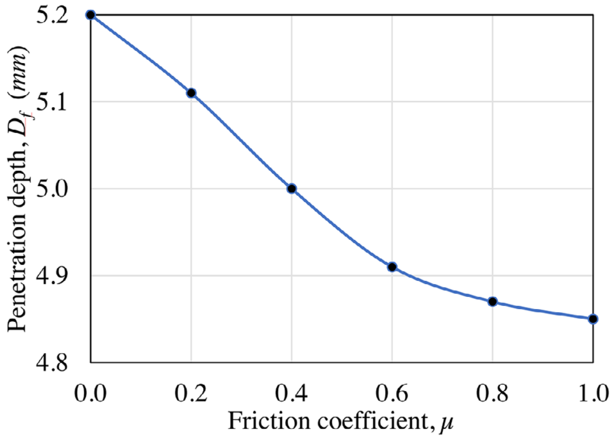

(A) Drop height = 0mm

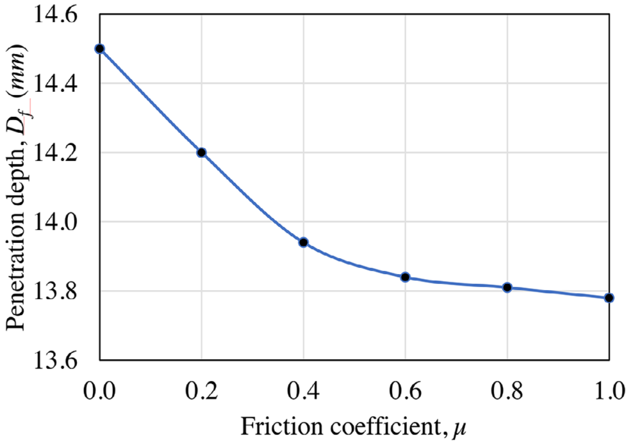

(B) Drop height = 20 mm

FIGURE 11 | Influence of the friction coefficient on the final penetration depth (D_f) of the free fall cone penetrometer (FFCP).

for the chosen grid size, is presented in Appendix C. The present analysis utilizes material parameters outlined in Table 6. According to the experimental findings depicted in Figure 7C, the FFCP requires between 0.01 and 0.02 s to reach the free-fall condition from the initial state. To replicate this behavior in the numerical simulation, the acceleration due to gravity is gradually increased from 0 to 0.01 s. Subsequently, beyond 0.01 s, the acceleration due to gravity remains constant at a fixed value of $9.81 \mathrm{m/s^2}$.

Figure 7A–C compare the development penetration depth, velocity, and acceleration over time between experimental observations and numerical simulations of the FFCPT when dropped from the soil surface. Figure 7A–C demonstrate that the numerical and experimental profiles of displacement, velocity, and acceleration associated with the cone penetration process match quite well. Figure 7D shows the variation of reaction force on FFCP with penetration depth during the FFCP penetration into the soil. Additionally, Table 4 presents the values of the final penetration depth, peak velocity, maximum deceleration, and maximum reaction force of the FFCP associated with numerical simulation. These parameters obtained from the numerical analysis align closely with experimental values. The difference between final penetration depths D_f associated with experimental and numerical simulations is smaller than 10%.

TABLE 6 | Material parameters for numerical simulation.

Parameters	Values
Related to FFCP	
Mass of FFCP, m(g)	60
Young's modulus, E (kPa)	210×10^6
Poisson's ratio, ν	0.3
Drop height, D_h(mm)	0, 10, 20
FFCP-soil interface friction coefficient, μ	0.7
Related to soil	
Soil density, ρ (kN/m^3)	14
Reference undrained Young's Modulus, $E_{u,ref}$ (kPa)	$500s_{u,ref}$
Poisson's ratio, ν	0.499
Reference undrained shear strength, $s_{u,ref}$ (kPa)	6.7
Reference shear strain rate, $\dot{\gamma}_{ref}(s^{-1})$	0.5
Strain rate parameter associated with power law, β	0.08
Sensitivity of soil, s_t	10
95% remoulded shear strain, γ_{95}	10

In the experiments, the cone reached its final penetration depth at roughly 0.06 s, whereas in the numerical simulation, it took around 0.055 s. The final penetration depth obtained from the numerical simulation (4.9 mm) is close to the average penetration depth obtained from the experiments (4.8 mm). Figure 7A also shows that the cone rebounded around 0.1–0.2 mm in the experiments. The numerical simulation shows a rebound of approximately 0.08 mm. Table 4 demonstrates that the numerical model predicts the maximum velocity to be approximately 0.181 m/s, which is close to the average maximum velocity from the experiment (0.18 m/s). Figure 7C shows that the numerical penetrometer acceleration oscillates upon completion of the penetration process, with the magnitude of these oscillations gradually diminishing over time. Since GIMP is an entirely explicit method that accounts for dynamic forces, it is presumed that these oscillations arise from the assumed elastic behavior of the material within the Tresca model at stress levels below yield. These effects become apparent due to the complete absence of numerical damping in the simulation, which enables a more accurate representation of the entire process dynamics.

Figure 7D shows the variation of reaction force on FFCP (Q) with the penetration depth during the penetration of the soil sample. Both the experimental and numerical simulations indicate that the reaction force is not zero at the onset of the simulation, which may be attributed to initial friction between the sleeve and the penetrometer. As the penetration depth increases, the cone reaction force exhibits a nonlinear growth pattern due to an increase in soil resistance. Experimental observations reveal that the maximum reaction force on the FFCP (Q_{max}) ranges from 1.14 to 1.27 N, while the numerically obtained value of Q_{max} is 1.25 N.

Figure 13A displays the displacement contour from the numerical simulation of the FFCPT with zero impact velocity. It illustrates

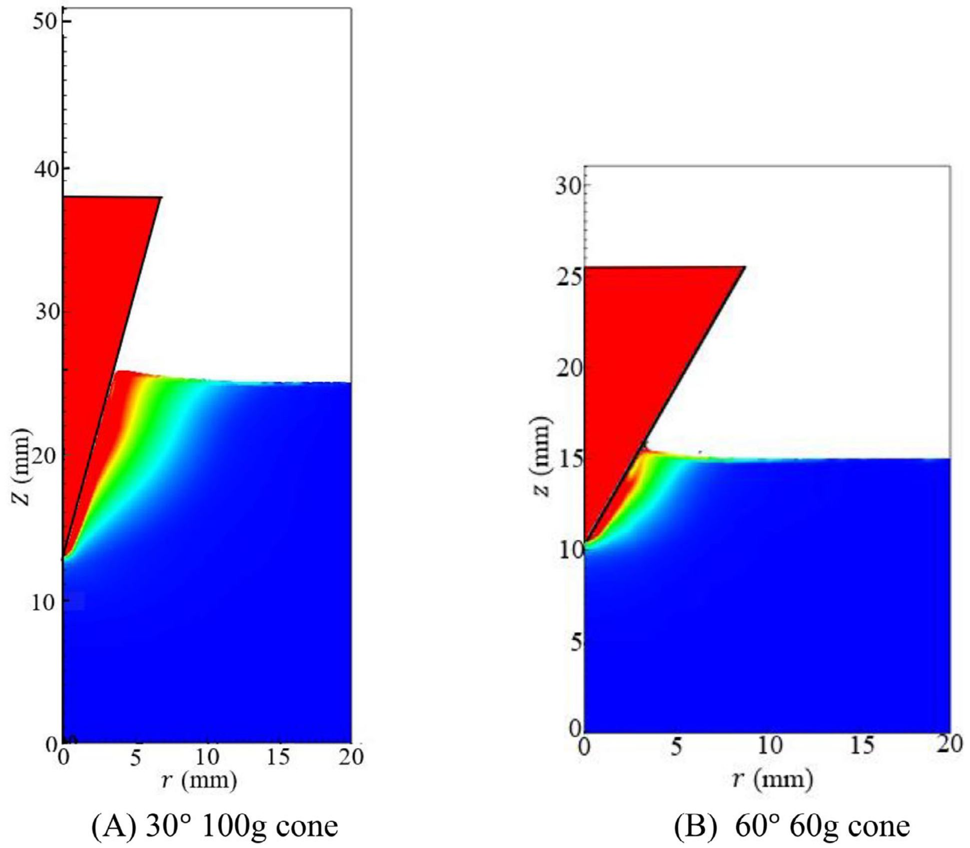

(A) 30° 100g cone

(B) 60° 60g cone

FIGURE 12 | The displacement contours of 30° and 60° cones at the end of cone penetration process.

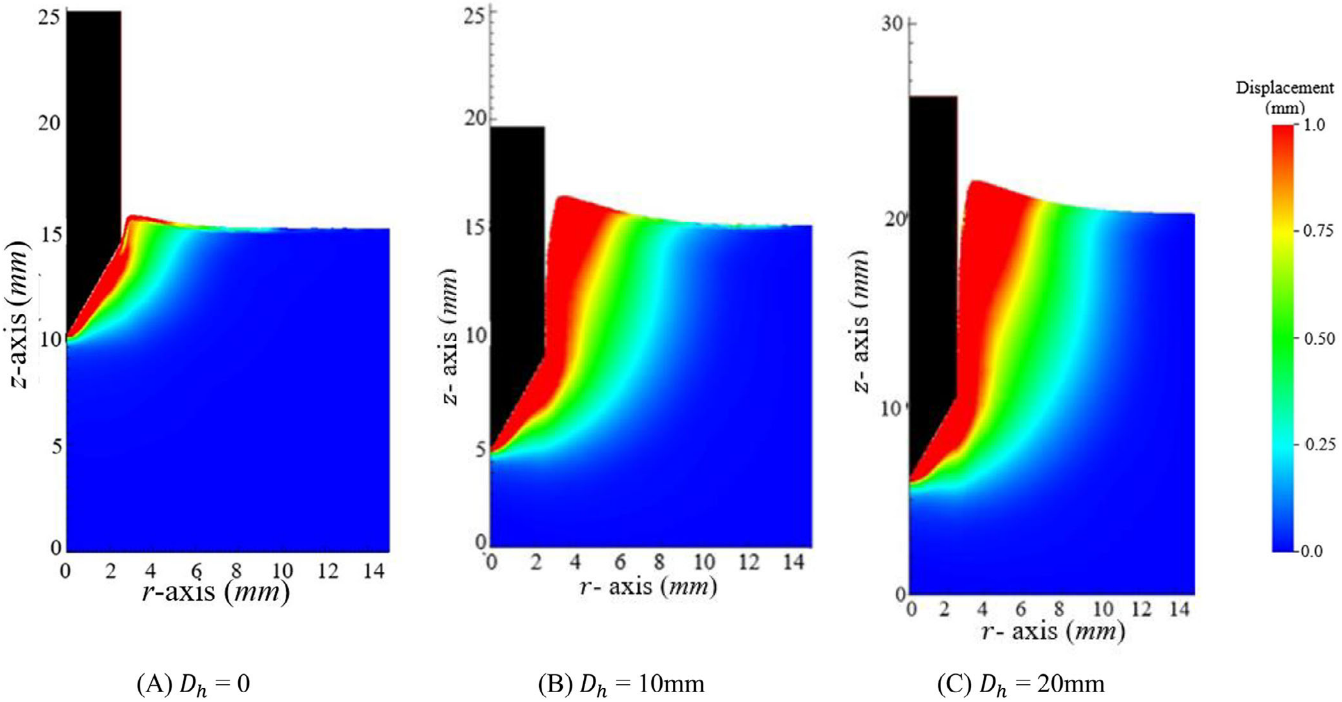

(A) D_h = 0

(B) D_h = 10mm

(C) D_h = 20mm

FIGURE 13 | The displacement contours associated with the free fall cone penetrometer (FFCP) dropped from different heights.

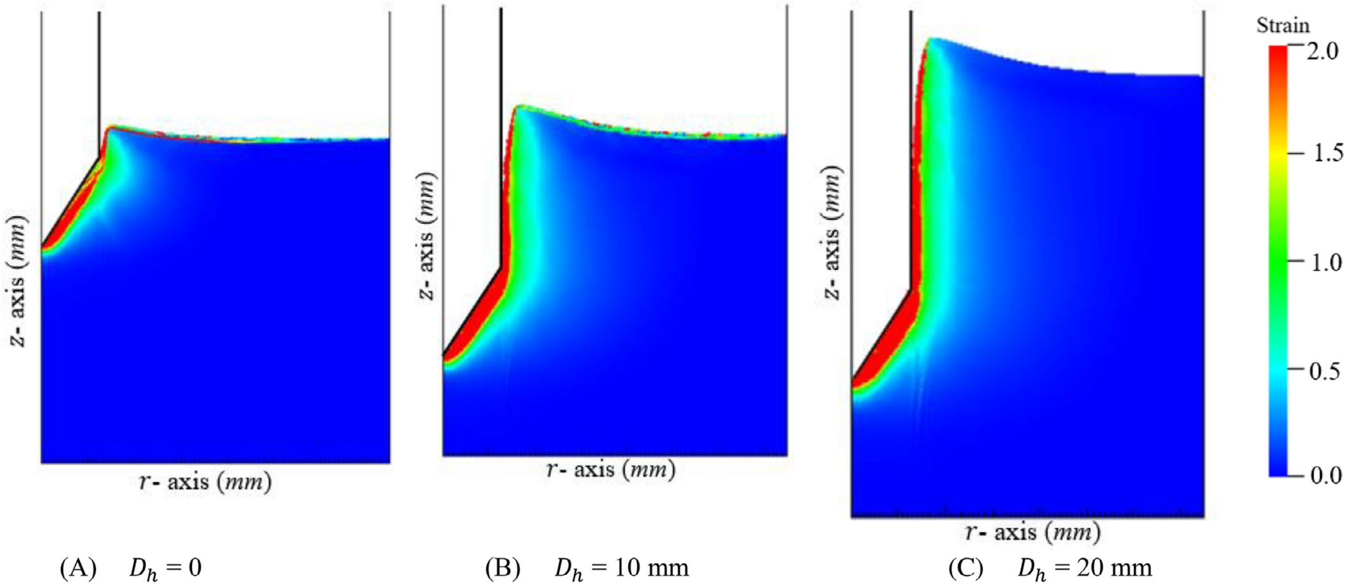

FIGURE 14 | Variation in pattern of shear strain at the end of the free fall cone penetrometer (FFCP) penetration process.

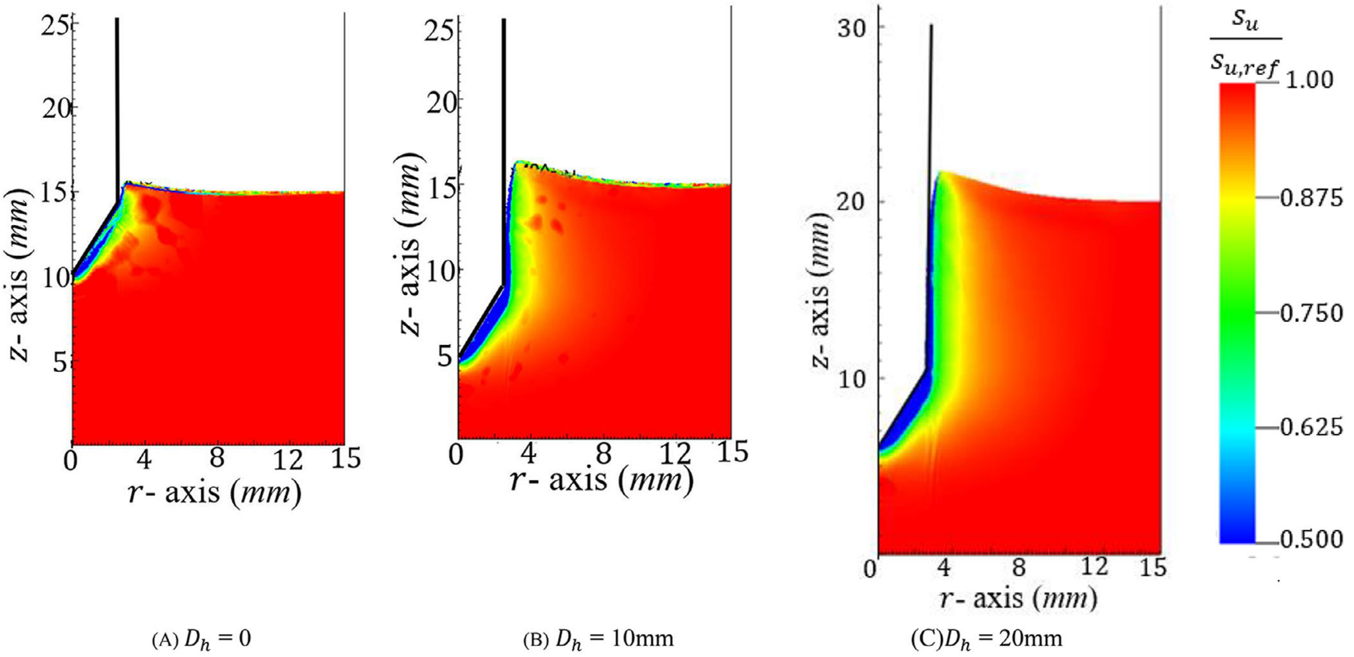

FIGURE 15 | The distribution of normalized undrained shear strength for different drop heights at the end of the free fall cone penetrometer (FFCP) penetration process.

that a small area of soil around the FFCP, spanning 6 mm horizontally, fails and moves upward, causing a heave at the soil surface as the FFCP penetrates into the soil. Figure 14A shows the variation of shear strain and Figure 15A shows the variation of normalized undrained shear strength ($s_u/s_{u,ref}$) after the FFCP penetration process [50].

4.2 | Numerical Simulation of FFCPTs With Initial Velocity

As explained in Section 3.3, the FFCP dropped from different drop heights ($D_h = 10$ and 20 mm) are numerically simulated by assigning the experimentally determined initial velocities as described in Table 3. Figures 8 and 9 compare the numerical displacement, velocity, acceleration, and reaction force of FFCP during penetration with the corresponding experimental data for D_h= 10 and 20 mm, respectively. Table 4 provides the values of the final penetration depth, peak velocity, maximum deceleration, and maximum reaction force of the FFCP associated with numerical simulation. As expected, values of these parameters increase with the increase in impact velocity (V_i). Figures 8 and 9 demonstrate that the numerical simulations closely match the experiments conducted with different impact velocities. The numerical simulation replicates well the penetration time of FFCP in soil and the slight rebound of FFCP

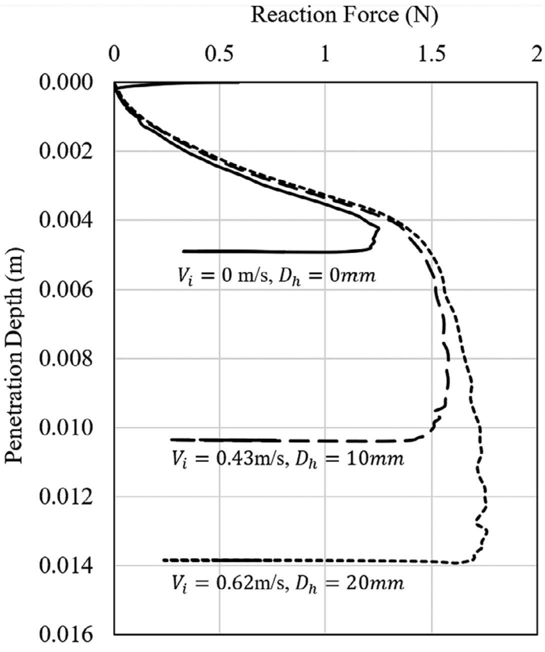

FIGURE 16 | Influence of impact velocity on free fall cone penetrometer (FFCPT) reaction force.

observed in the experiments. Furthermore, the final penetration depth, peak velocity, maximum deceleration, and maximum reaction force values obtained through numerical simulation closely match their experimental counterparts. However, we observed that the numerical acceleration curve associated with the case D_h= 20 mm (Figure 9C) does not match very well the experimental acceleration curves. The difference between the peaks of the experimental average and numerical data is around 16% (see Table 4). The experimental acceleration curves are obtained by numerically double differentiating the displacement curves. Furthermore, various smoothing techniques are used for numerical differentiation (refer to Appendix A). Therefore, the experimental acceleration curves may not be highly accurate. Similarly, the numerical acceleration curves are obtained by numerically differentiating the displacement curves derived from MPM analysis. This difference in peaks may be attributed to the methodology used for obtaining the acceleration curves.

Figure 16 compares the reaction force on the FFCP during penetration at various impact velocities. Figure 16 shows that after the FFCP penetrates soil the reaction force on FFCP increases rapidly in a nonlinear manner and reaches a stable value at a penetration depth around 4–5 mm. As the FFCP penetrates the soil further, the soil near the cone remoulds gradually. That may be the reason for the reduction in the rate of increase of reaction force on the FFCP (see Figure 17). The maximum reaction force (Q_{max}) on the FFCP associated with D_h= 0, 10 and 20 mm are found to be 1.25, 1.58, and 1.76 N, respectively. Figure 16 also confirms that the reaction force on FFCP increases with an increase in impact velocity. This is mainly because the undrained shear strength of the soil increases with an increase in localized shear strain rate when the FFCP impacts the soil with higher velocity. This results in increased soil resistance and a higher reaction force on the FFCP.

Figure 13 shows the displacement contours associated with FFCPT numerical simulation. It reveals a curvilinear failure pattern emerging near the FFCP. The soil surrounding FFCP moves upward after failure as the FFCP penetrates the soil, resulting in a heave at the soil surface. As the penetration depth increases, the lateral extent of the failed soil zone also expands, leading to a corresponding increase in the heave at the soil surface. Additionally, a small gap develops between the soil and the FFCP near the soil surface as the FFCP penetrates deeper. Furthermore, Figure 13 demonstrates that the lateral extent of failed soil is concentrated within 6, 8, and 10 mm from the center of the FFCP for D_h= 0, 10, and 20 mm, respectively.

Figure 14 displays the distribution of accumulated plastic shear strain in the soil around the FFCP at the end of the penetration process. It reveals that plastic shear strains are predominantly accumulated in a thin soil zone close to the FFCP, while penetrating. During the process of FFCP penetration, the plastic shear strain also accumulates near the soil zone close to the cone tip. Figure 15 shows the distribution of normalized undrained shear strength ($s_u/s_{u,ref}$), obtained from the numerical simulation of the FFCPT, for different drop heights at the end of the penetration process. This demonstrates the formation of a thin shear band (blue zone), around the FFCP, where severe strain softening occurs. Within this blue zone, the undrained shear strength of the soil is less than 50% of the reference undrained shear strength of the soil. For a more detailed understanding of the mechanisms involved in these numerical simulations, please refer to Appendix A.

4.3 | Influence of Strain Rate and Strain Softening on FFCP Penetration Process

The reaction force (Q) and the final penetration depth (D_f) of the FFCP is highly dependent on the soil resistance during the penetration process. Soil resistance, or undrained shear strength of soil during the FFCP penetration process, depends on strain rate and strain softening behavior of the surrounding soil. To gain further insight into the effect of strain rate and strain softening on the penetration process, additional numerical simulations are conducted in this section. A numerical simulation of FFCPT is performed by considering the effect of strain softening and strain rate (with parameters set as s_t = 10, γ_{95} = 10 and β= 0.08), and another simulation is conducted without considering the effect of strain softening (with parameters set as s_t = 1, $\gamma_{95} = \infty$ and β= 0.08) for D_h = 20 mm. Figure 17 depicts the contour plots of the undrained shear strength of the soil normalized with the reference undrained shear strength of the soil ($s_u/s_{u,ref}$) associated with these two cases at t = 0.01 and 0.02 s after penetration starts. Figure 17 illustrates that in the case where strain softening is not considered in the analysis, the undrained shear strength of the soil around the FFCP increases because of the high localized strain rates generated during the penetration process. In contrast, when both strain rate effects and strain softening are considered, a shear band starts to form in a small region of soil near the FFCP at t = 0.01 seconds. This shear band forms due to the accumulation of plastic strain in the soil. As the cone penetrates further, at t = 0.02s, more surrounding soil is further remoulded, and a visible shear band forms in the soil adjacent to the FFCP. This reduction in soil strength ultimately

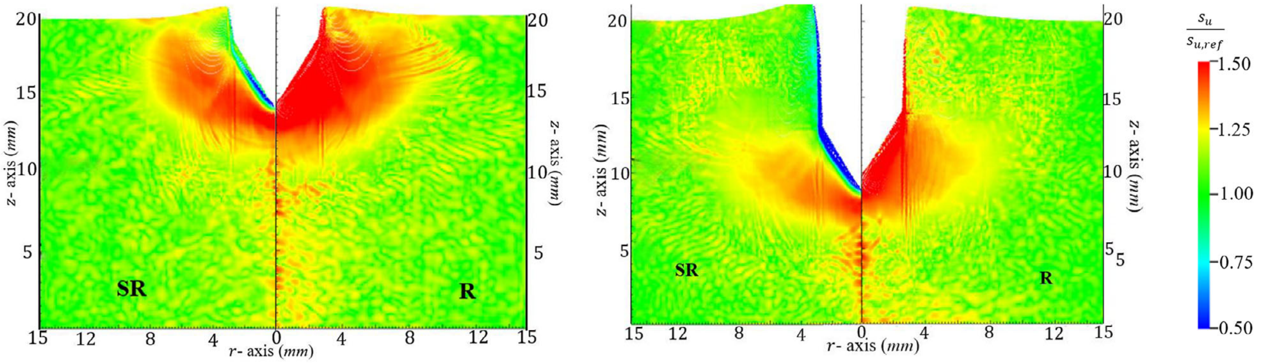

(A) t= 0.01s

(B) t = 0.02s

FIGURE 17 | The distribution of normalized undrained shear strength for 20 mm drop height during the free fall cone penetrometer (FFCP) penetration process. SR—Considering both strain rate and strain softening (destructuration) effect. R—Considering only strain rate effect.

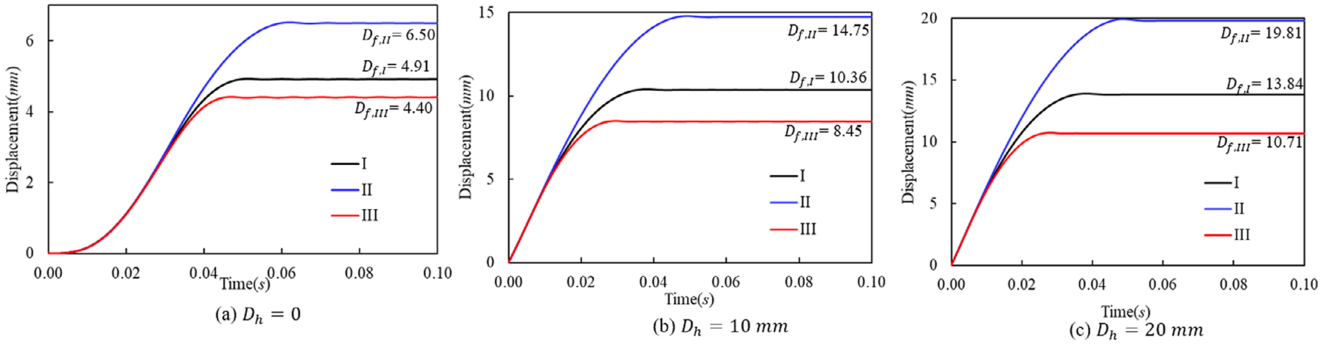

(a) $D_h = 0$

(b) $D_h = 10\ mm$

(c) $D_h = 20\ mm$

FIGURE 18 | Effect of strain rate and sensitivity on the FFCP displacement during cone penetration process. (I) Considering both strain rate and strain softening effect. (II) Considering only strain softening effect. (III) Considering only strain rate effect.

leads to an increase in penetration depth compared to the first case. The spread of the plastic soil zone is bigger in the first case. This indicates that interpreting undrained shear strength based on FFCPT without considering the strain softening effect will result in underestimating the actual undrained shear strength of the soil. Figure 17 depicts a checkerboard pattern variation of $s_u/s_{u,ref}$ across the entire soil domain. This pattern primarily correlates with the strain rate, which, in turn, arises from dynamic simulation and the propagation of elastic waves through the material. Development of $s_u/s_{u,ref}$ during the whole process of the numerical simulation of the above two cases are presented in video formats in Supporting Information.

Furthermore, to investigate the effects of strain softening and strain rate, FFCPT numerical simulations were conducted for three distinct cases: (I) considering both strain rate and strain softening effects, (II) considering only the strain softening effect (not considering strain rate effect), and (III) considering only the strain rate effect (not considering strain softening effect). These numerical simulations were performed for three different drop heights: (a) D_h= 0 mm, (b) D_h= 10 mm, and (c) D_h = 20 mm. Figure 18 displays the displacement versus time profile associated with these cases. It demonstrates that strain softening, and shear strain rate significantly influence the displacement profile of the FFCP during the penetration process and the final penetration depth (D_f) of the FFCP. By not considering the strain rate effect the final penetration depth of the FFCP can deviate from the actual solution (Case I) by 30% for D_h= 0%–40% for D_h= 20 mm. Similarly, not considering strain softening overestimates the final penetration depth by 10% for D_h= 0% –22% for D_h= 20 mm. Both the effects of strain rate and strain softening are more pronounced for cases involving larger drop heights or higher impact velocities. This is primarily due to the higher shear strain rate and greater accumulation of plastic strain associated with the numerical simulations of larger drop heights. This suggests that in deep penetration processes, such as in situ CPT or FFCPT, the influence of strain rate and strain softening will be more substantial

5 | Conclusions

This paper investigates the dynamic penetration process of a model FFCP in marine clay. The paper presented an extensive set of experimental results on marine clay samples. Then the study introduced a numerical framework capable of simulating the FFCP penetration in marine clay using the MPM. Based on numerical simulations, it appears that the high strain rate and destructuration behavior of clay are important phenomena affecting the penetration depth. These effects are well captured by an extended Tresca material model, allowing for very good replication of the experimental data with the GIMP simulations. The material parameters associated with strain rate and destructuration used are the same as those used in Mohapatra et al. [25] for replication of fall cone experiments done with similar soils. The study examines the effect of impact velocity, FFCP roughness, mesh density, strain rate, and strain softening on the FFCP penetration process. The key outcomes of this study are outlined below:

1. The study provides well-controlled laboratory-scale FFCPT experimental data, including FFCPT displacement, velocity, acceleration, and reaction force profiles obtained during the FFCP penetration process. The data also includes other laboratory tests useful for parameterizing constitutive models for soil. Altogether, the data could be used for the validation of numerical tools intended for simulating in situ FFCPT tests.
2. The numerical framework utilized in this study effectively reproduces the laboratory-scale FFCPT experimental results. The displacement, velocity, acceleration, and reaction force curves obtained from the numerical simulations closely align with the experimental curves during the FFCP penetration process.
3. The numerical simulation results indicate that by using the undrained shear strength obtained from the triaxial experiment and incorporating the strain rate and strain softening parameters as reported in Mohapatra et al. [25], the GIMP simulations using a dense grid can replicate the mechanisms relevant to the penetration of the FFCP into the offshore Finnish clay. This provides the confidence that similar replication may be possible in large-scale simulations such as the in situ free fall cone test (FFCPT).
4. The strain rate and strain softening significantly impact the FFCP penetration process. Numerical results indicate that neglecting the strain rate effect may lead to an underestimation of the final penetration depth by 30%–40%, while disregarding strain softening may result in an overestimation of the final penetration depth by 10%–22%. Moreover, the simulation highlights that these effects are more pronounced when the cone is dropped from a greater height or with a higher impact velocity. Therefore, for in situ FFCPT simulations, where the impact velocity is approximately 10 m/s, both the strain rate and strain softening effects should be considered.
5. The numerical simulations show that during the FFCP penetration process, a shear band is formed very close to the soil surrounding the FFCP. In that region, the strain softening behavior has a significant influence, which reduces the undrained shear strength value of the soil in that region.
6. It is essential to use a numerical method that can take into account shear band thickness to achieve convergence of the results with mesh density increase
7. The reaction force on the FFCP, commonly used to estimate the undrained shear strength of soil in in-situ FFCPT, is significantly influenced by the strain rate and strain softening behavior of the surrounding soil. Thus, when interpreting the undrained shear strength of soil from FFCPT data, it is essential to consider both the effects of strain rate and strain softening.

Nomenclature

FFCPT	free fall cone penetrometer test
FFCP	free fall cone penetrometer
FCT	fall cone test
s_u	undrained shear strength
D_f	final penetration depth of FFCP
D_h	drop height
V_p	peak velocity
D_{max}	maximum deceleration
Q_{max}	maximum reaction force
ρ	soil density
ρ_s	particle density
W	water content
s_t	sensitivity
q	deviatoric stress
ε_a	axial strain
Q	reaction force
W	weight of the FFCP
m	mass of the FFCP
a	acceleration of the FFCP
V_i	impact velocity of the FFCP
t_i	impact time
G_u	undrained shear modulus
$G_{u,ref}$	reference undrained shear modulus
$\dot{\gamma}$	shear strain rate
γ	accumulated shear strain
$\dot{\gamma}_{ref}$	reference shear strain
$s_{u,ref}$	reference undrained shear strength at $\delta\gamma_{ref}$
μ	friction coefficient
$E_{u,ref}$	reference undrained Young's modulus of soil
ν	Poisson's ratio
β	strain rate parameter associated with power law
γ_{95}	95% remoulded shear strain
h	grid size
$s_u/s_{u,ref}$	normalized undrained shear strength

Acknowledgments

This project has received funding from the European Union—NextGenerationEU instrument and is funded by the Research Council of Finland under grant number 347602. This study has utilized research infrastructure facilities provided by the Finnish Marine Research Infrastructure (FINMARI) network.

Data Availability Statement

The data that supports the findings of this study are available in the supplementary material of this article.

References

1. S. H. Chow and D. W. Airey, "Soil Strength Characterisation Using Free-Falling Penetrometers," *Geotechnique* 63, no. 13 (2013): 1131–1143.

2. M. Saresma, J. J. Virtasalo, Z. S. Li, D. Mohapatra, and W. Sołowski, "In Situ Free-Fall Cone Penetrometer (FF-CPT) and Laboratory Fall Cone Characterisation of Soft Marine Sediments in the Gulf of Finland, Baltic Sea," in *Offshore Site Investigation Geotechnics 9th International Conference Proceeding*, vol. 1911, no. 1918, Society for Underwater Technology, pp. 1911–1918, 2023, https://doi.org/10.3723/DSES3939.

3. J. Paprocki, N. Stark, and T. Lippmann, "Geotechnical Characterization of a Tidal Estuary Mudflat Using Portable Free-Fall Penetrometers," *Journal of Geotechnical and Geoenvironmental Engineering* 150, no. 1 (2024): 04023131.

4. N. Stark, N. Parasie, and J. Peuchen, "Deepwater Soil Investigation Using a Free Fall Penetrometer," *Canadian Geotechnical Journal* 59, no. 12 (2022): 2196–2201.

5. J. Rong, M. Nazem, S. H. Chow, A. Zhou, and S. Moridpour, "Design and Application of Dynamic Seabed Penetrators in Offshore Geotechnical Engineering: A Review," *Ocean Engineering* 293 (2024): 116599, https://doi.org/10.1016/J.OCEANENG.2023.116599.

6. N. Stark, R. Wilkens, V. B. Ernstsen, M. Lambers-Huesmann, S. Stegmann, and A. Kopf, "Geotechnical Properties of Sandy Seafloors and the Consequences for Dynamic Penetrometer Interpretations: Quartz Sand versus Carbonate Sand," *Geotechnical and Geological Engineering* 30, no. 1 (2012): 1–14, https://doi.org/10.1007/S10706-011-9444-7/TABLES/5.

7. C. P. Aubeny and H. Shi, "Interpretation of Impact Penetration Measurements in Soft Clays," *Journal of Geotechnical and Geoenvironmental Engineering* 132, no. 6 (2006): 770–777, https://doi.org/10.1061/(ASCE)1090-0241(2006)132:6(770).

8. D. J. White, C. D. O'Loughlin, N. Stark, and S. H Chow, "Free Fall Penetrometer Tests In Sand: Determining the Equivalent Static Resistance," in *Proceedings of the 4th International Symposium on Cone Penetration Testing* (Delft, Netherlands, 2018), 695–701.

9. M. Nazem, J. P. Carter, D. W. Airey, and S. H. Chow, "Dynamic Analysis of a Smooth Penetrometer Free-Falling Into Uniform Clay," *Geotechnique* 62, no. 10 (2012): 893–905, https://doi.org/10.1680/GEOT.10.P.055.

10. M. H. Moavenian, M. Nazem, J. P. Carter, and M. F. Randolph, "Numerical Analysis of Penetrometers Free-Falling Into Soil With Shear Strength Increasing Linearly With Depth," *Computers and Geotechnics* 72 (2016): 57–66, https://doi.org/10.1016/J.COMPGEO.2015.11.002.

11. S. H. Chow, A. M. Asce, and D. W. Airey, "Free-Falling Penetrometers: A Laboratory Investigation in Clay," *Journal of Geotechnical and Geoenvironmental Engineering* 140, no. 1 (2014): 201–214, https://doi.org/10.1061/(ASCE)GT.1943-5606.0000973.

12. P. J. Mulhearn, J. Boyle, and G. Crook, *Sediment Properties off Cairns (A Report on Data obtained in August 1996)* (Science and Technology Organisation Technical Note DSTO-TN-0154. Department of Defence (Australia, 1998), 53, https://apps.dtic.mil/sti/citations/ADA355873.

13. L. Bowman, R. March, P. Orenberg, D. True, and H. Hermann, "Evaluation of Dropped Versus Static Cone Penetrometers at a Calcareous Cohesive Site," *Oceans Conference Record (IEEE)* 3 (1995): 1846–1858, https://doi.org/10.1109/OCEANS.1995.528862.

14. R. M. Bread, "Expendable Doppler Penetrometer: A Performance Evaluation," *Civil Engineering Laboratory, Naval Construction Battalion Center* (1977).

15. U. Dayal and J. H. Allen, "Instrumented Impact Cone Penetrometer," *Canadian Geotechnical Journal* 10, no. 3 (1973): 397–409, https://doi.org/10.1139/t73-034.

16. D. Elsworth and D. S. Lee, "Indentation of a Free-Falling Lance Penetrometer Into a Poroelastic Seabed," *International Journal for Numerical and Analytical Methods in Geomechanics* 29, no. 2 (2005): 141–162, https://doi.org/10.1002/NAG.408.

17. S. H. Chow, C. D. O'Loughlin, D. J. White, and M. F. Randolph, "An Extended Interpretation of the Free-Fall Piezocone Test in Clay," *Geotechnique* 67, no. 12 (2017): 1090–1103, https://doi.org/10.1680/JGEOT.16.P.220.

18. S. H. Chow, C. D. O'Loughlin, C. L. V. Goh, R. McIlduff, D. J. White, and F. C. Chow, "A Comparative Field Study of Free-Fall Cone and Sphere Penetrometers in Soft Sediment," *Ocean Engineering* 280 (2023): 114094, https://doi.org/10.1016/J.OCEANENG.2023.114094.

19. L. Zambrano-Cruzatty and A. Yerro, "Numerical Simulation of a Free Fall Penetrometer Deployment Using the Material Point Method," *Soils and Foundations* 60, no. 3 (2020): 668–682, https://doi.org/10.1016/J.SANDF.2020.04.002.

20. A. Abelev, K. Tubbs, and P. Valent, "Numerical Investigation of Dynamic Free-fall Penetrometers in Soft Cohesive Marine Sediments Using a Finite Difference Approach," in *MTS/IEEE Biloxi—Marine Technology for Our Future: Global and Local Challenges, OCEANS* (2009), https://doi.org/10.23919/OCEANS.2009.5422350.

21. D. Mohapatra, M. Saresma, J. Virtalaso, and W. Sołowski, "Numerical Simulation of a Laboratory-Scale Free Fall Cone Penetrometer Test in Marine Clay With the Material Point Method," in *VIII International Conference on Particle-Based Methods* (CIMNE, 2023).

22. B. C. Thomas Sheahan, C. C. Ladd, H. Member, and J. T. Germaine, "Rate-Dependent Undrained Shear Behavior of Saturated Clay," *Journal of Geotechnical Engineering* 122, no. 2 (1996): 99–108, https://doi.org/10.1061/(ASCE)0733-9410(1996)122:2(99).

23. Q. A. Tran and W. Sołowski, "Generalized Interpolation Material Point Method Modelling of Large Deformation Problems Including Strain-Rate Effects—Application to Penetration and Progressive Failure Problems," *Computers and Geotechnics* 106 (2019): 249–265, https://doi.org/10.1016/J.COMPGEO.2018.10.020.

24. N. Boukpeti, D. J. White, M. F. Randolph, and H. E. Low, "Strength of Fine-Grained Soils at the Solid-Fluid Transition," *Geotechnique* 62, no. 3 (2012): 213–226, https://doi.org/10.1680/GEOT.9.P.069.

25. D. Mohapatra, S. Mohammadi, M. Saresma, J. Virtasalo, and W. Sołowski, "Fall Cone Tests on Sensitive Marine Clay: A Comprehensive Experimental Study and Its Replication with the Generalized Interpolation Material Point Method," 25 November 2024, PREPRINT (Version 1), https://doi.org/10.21203/rs.3.rs-5500388/v1.

26. P. Alenius, "The Physical Oceanography of the Gulf of Finland: A Review," *Boreal Environment Research* 3, no. 2 (1998).

27. J. J. Virtasalo, A. T. Kotilainen, M. E. Räsänen, and A. K. Ojala, "Late-Glacial and Post-Glacial Deposition in a Large, Low Relief, Epicontinental Basin: The Northern Baltic Sea," *Sedimentology* 54, no. 6 (2007): 1323–1344, https://doi.org/10.1111/J.1365-3091.2007.00883.X.

28. J. J. Virtasalo, J. Hämäläinen, and A. T. Kotilainen, "Toward a Standard Stratigraphical Classification Practice for the Baltic Sea Sediments: The CUAL Approach," *Boreas* 43, no. 4 (2014): 924–938, https://doi.org/10.1111/BOR.12076.

29. R. Khalili, C. Jommi, and W. T. Sołowski, "Impact of a Spacing Reduction in a Fall Cone Test," in *Geotechnical Engineering Challenges to Meet Current and Emerging Needs of Society* (CRC Press, 2024), 1679–1683.

30. J. Shi and C. Tomasi, "Good Features to Track," in *Proceedings of the IEEE Computer Society Conference on Computer Vision and Pattern Recognition* (1994), 593–600, https://doi.org/10.1109/CVPR.1994.323794.

31. C. Tomasi and T. Kanade, "Shape and Motion From Image Streams: A Factorization Method," *Proceedings of the National Academy of Sciences of the United States of America* 90 (1993): 9795–9802.

32. D. Mohapatra, Z. Li, M. Saresma, J. Virtasalo, and W. Solowski, "Replication of Fall Cone Test on Marine Clay With a Generalized Interpolation Material Point Method Simulation," in *10th European Conference on Numerical Methods in Geotechnical Engineering* (2023), 1–7, https://doi.org/10.53243/NUMGE2023-289.

33. D. Sulsky, S. J. Zhou, and H. L. Schreyer, "Application of a Particle-in-Cell Method to Solid Mechanics," *Computer Physics Communications* 87, no. 1–2 (1995): 236–252, https://doi.org/10.1016/0010-4655(94)00170-7.

34. D. Sulsky, Z. Chen, and H. L. Schreyer, "A Particle Method for History-Dependent Materials," *Computer Methods in Applied Mechanics*

and Engineering 118, no. 1–2 (1994): 179–196, https://doi.org/10.1016/0045-7825(94)90112-0.

35. D. Z. Zhang, X. Ma, and P. T. Giguere, "Material Point Method Enhanced by Modified Gradient of Shape Function," *Journal of Computational Physics* 230, no. 16 (2011):6379–6398, https://doi.org/10.1016/J.JCP.2011.04.032.

36. A. Sadeghirad, R. M. Brannon, and J. E. Guilkey, "Second-Order Convected Particle Domain Interpolation (CPDI2) With Enrichment for Weak Discontinuities at Material Interfaces," *International Journal for Numerical Methods in Engineering* 95, no. 11 (2013): 928–952, https://doi.org/10.1002/NME.4526.

37. S. G. Bardenhagen and E. M. Kober, "The Generalized Interpolation Material Point Method," *Computer Modeling in Engineering and Sciences* 5, no. 6 (2004): 477–496, https://doi.org/10.3970/cmes.2004.005.477.

38. I. Einav and M. Randolph, "Effect of Strain Rate on Mobilised Strength and Thickness of Curved Shear Bands," *Geotechnique* 56, no. 7 (2006): 501–504.

39. S. W. Jeong, S. Leroueil, and J. Locat, "Applicability of Power Law for Describing the Rheology of Soils of Different Origins and Characteristics," *Canadian Geotechnical Journal* 46, no. 9 (2009): 1011–1023.

40. H. Zhou and M. F. Randolph, "Resistance of Full-Flow Penetrometers in Rate-Dependent and Strain-Softening Clay," *Geotechnique* 59, no. 2 (2009): 79–86.

41. K. K. Sorensen, B. A. Baudet, and B. Simpson, "Influence of Strain Rate and Acceleration on the Behaviour of Reconstituted Clays at Small Strains," *Geotechnique* 60, no. 10 (2010): 751–763.

42. T. Quinn, "Rate Effects in Fine Grained Soils" (PhD Thesis, University of Dundee, 2013).

43. J. A. Nairn, C. C. Hammerquist, and G. D Smith, "New Material Point Method Contact Algorithms for Improved Accuracy, Large-Deformation Problems, and Proper Null-Space Filtering," *Computer Methods in Applied Mechanics and Engineering* 362 (2020): 112859, https://doi.org/10.1016/J.CMA.2020.112859.

44. J. Guilkey, R. Lander, and L. Bonnell, "A Hybrid Penalty and Grid Based Contact Method for the Material Point Method," *Computer Methods in Applied Mechanics and Engineering* 379 (2021): 113739, https://doi.org/10.1016/J.CMA.2021.113739.

45. J. G. Potyondy, "Skin Friction Between Various Soils and Construction Materials," *Géotechnique* 11, no. 4 (1961): 339–353, https://doi.org/10.1680/geot.1961.11.4.339.

46. Y. Tsubakihara, H. Kishida, and T. Nishiyama, "Friction Between Cohesive Soils and Steel," *Soils and Foundations* 33, no. 2 (1993): 145–156, https://doi.org/10.3208/SANDF1972.33.2_145.

47. T. Koumoto and G. T. Houlsby, "Theory and Practice of the Fall Cone Test," *Géotechnique* 51, no. 8 (2001): 701–712, https://doi.org/10.1680/geot.51.8.701.40475.

48. W. M. Coombs, T. J. Charlton, M. Cortis, and C. E. Augarde, "Overcoming Volumetric Locking in Material Point Methods," *Computer Methods in Applied Mechanics and Engineering* 333 (2018): 1–21, https://doi.org/10.1016/J.CMA.2018.01.010.

49. C. M. Mast, P. Mackenzie-Helnwein, P. Arduino, G. R. Miller, and W. Shin, "Mitigating Kinematic Locking in the Material Point Method," *Journal of Computational Physics* 231, no. 16 (2012): 5351–5373, https://doi.org/10.1016/J.JCP.2012.04.032.

50. K. Soga, E. Alonso, A. Yerro, K. Kumar, and S. Bandara, "Trends in Large-Deformation Analysis of Landslide Mass Movements With Particular Emphasis on the Material Point Method," *Geotechnique* 66, no. 3 (2016): 248–273, https://doi.org/10.1680/JGEOT.15.LM.005.

51. J. Oliver and A. E. Huespe, "Continuum Approach to Material Failure in Strong Discontinuity Settings," *Computer Methods in Applied Mechanics and Engineering* 193, no. 30–32 (2004): 3195–3220, https://doi.org/10.1016/J.CMA.2003.07.013.

52. N. M. Pinyol, M. Alvarado, E. E. Alonso, and F. Zabala, "Thermal Effects in Landslide Mobility," *Geotechnique* 68, no. 6 (2018): 528–545, https://doi.org/10.1680/JGEOT.17.P.054.

Supporting Information

Additional supporting information can be found online in the Supporting Information section.

Appendix A: Supplementary Materials

The MP4 videos of the laboratory scale FFCPT tests, conducted with drop heights (D_h) of 0 mm, 10 mm, and 20 mm, are labeled as follows: E-CP0-1 to E-CP0-5 for 0 mm, E-CP1-1 to E-CP1-5 for 10 mm, and E-CP2-1 to E-CP2-5 for 20 mm. The MP4 videos of the fall cone tests, conducted using a 30° 100 g cone and a 60° 60 g cone are labelled as E-30-1 to E-30-5 and E-60-1 to E-60-5, respectively. These videos correspond to the laboratory test programs described in Section 2.6.

The MATLAB script 'Track_FFCP.m' is used to determine the displacement, velocity, acceleration, and reaction force during the FFCP penetration process by applying MATLAB image processing techniques, as described in Section 2.5. The displacement, velocity, acceleration, and reaction force data for the FFCPT tests with drop heights (D_h) of 0 mm, 10 mm, and 20 mm are reported in the Excel spreadsheets E-CP0.xlsx, E-CP1.xlsx, and E-CP2.xlsx, respectively. These spreadsheet data correspond to the laboratory test programs described in Section 2.6 and are also linked to Figures 7, 8, and 9.

The development of displacement, plastic strain, and normalized undrained shear strength $(s_u/s_{u,\,ref})$ in the soil during the FFCP penetration process, based on numerical studies with drop heights (D_h) of 0 mm, 10 mm, and 20 mm, are presented in video format in the supplementary materials. The videos are labelled as follows: Disp-Dh0.mpg to Disp-Dh20.mpg for displacement, strain-Dh0.mpg to strain-Dh20.mpg for plastic strain, and nSu-Dh0.mpg to nSu-Dh20.mpg for normalized undrained shear strength. These videos correspond to numerical simulation results described in Section 4.

The videos depicting the development of displacement in the soil during the 30° and 60° cone penetration processes, based on numerical studies, are provided in the supplementary materials and labelled as Disp-30d.mpg and Disp-60d.mpg. These videos correspond to Section 3.4 and Figure 11.

The development of displacement in the soil during the FFCP penetration process with different grid densities is presented in the supplementary material as video files ranging from Dh0-MS0.8.mpg to Dh20-MS0.05.mpg. These videos are linked to Appendix C and Figure C2.

The numerical simulation results for displacement, velocity, acceleration, and reaction force during the FFCPT tests with drop heights (D_h) of 0 mm, 10 mm, and 20 mm are recorded in the Excel spreadsheets E-CP0.xlsx, E-CP1.xlsx, and E-CP2.xlsx, respectively. These data are linked to Figures 7, 8, and 9.

The development of normalized undrained shear strength $(s_u/s_{u,\,ref})$ throughout the numerical simulation process is presented in the supplementary materials as video files labelled R_Dh20.mpg and SR_Dh20.mpg, corresponding to the cases that consider only the rate effect and both the rate effect and strain softening, respectively. These videos are corresponding to Section 4.3 and Figure 17. Additionally, the displacement data for three scenarios: (I) considering both strain rate and strain softening effects, (II) considering only strain softening, and (III) considering only strain rate for D_h values of 0 mm, 10 mm, and 20 mm (as shown in Figure 18) are provided in the Excel spreadsheet SR-R.xlsx.

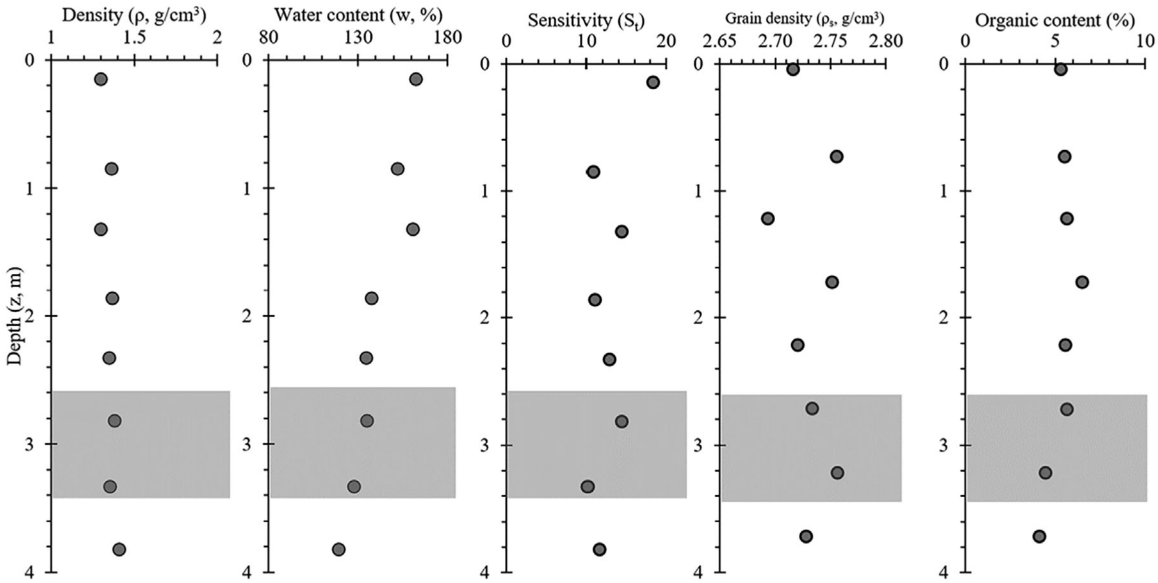

FIGURE B1 | Profile of the geotechnical index properties of Kytö clay.

TABLE B1 | Compressibility parameters obtained from the Oedometer tests.

Parameter	Soil Sample-1	Soil Sample-2
Depth (m)	2.60-2.62	3.98-4.00
Slope of NCL, λ	0.449	0.400
Slope of swelling line, κ	0.0953	0.0921
Compression Index, Cc	1.034	0.921
Recompression Index, C_r	0.219	0.212

Appendix B: Properties of Kytö Clay

This appendix presents additional soil properties for Kytö clay, derived from laboratory tests on soil samples from core MGKU-2022-2B. It provides a summary of the density, water content, sensitivity, and organic content of the soil along the depth, as illustrated in Figure B1. The grey area in the figure highlights the soil depth range used in this study. The CRS (constant rate of strain) oedometer test was performed on two soil samples from different depths: (a) Soil sample 1: from 2.60 to 2.62 meters and (b) Soil sample 2: from 3.98 to 4.00 meters. The e-ln (σ'_v) curves from these tests are shown in Figure B2. The compressibility parameters calculated from these curves are summarized in Table B1.

Appendix C: Mesh Sensitivity

The grid density and number of material points significantly influence the numerical simulation of the Generalized Interpolation Material Point Method. As discussed in Section 3.4, this analysis applies a scaling law to reduce the effects of mesh dependency [23, 54]. To investigate how the grid density impacts the simulation results, the analysis discretizes the problem domain in Figure C2 by using a structured mesh of square sizes $(h \times h)$ where $h = 0.8, 0.4, 0.2, 0.1$ and 0.05 mm, each time with 4 material points in the cell. These correspond to 1637, 6538, 25711, 102843 and 411368 material points in the simulation of FFCPT for drop height $(D_h) = 0$ mm, and 2171, 8763, 34461, 137843, 551368 material points in the simulation of FFCPT for drop height $(D_h) = 20$ mm. The final penetration depth (D_f) obtained from the above numerical simulations is used as a representative parameter to study the influence of grid density. Figure C1 demonstrates

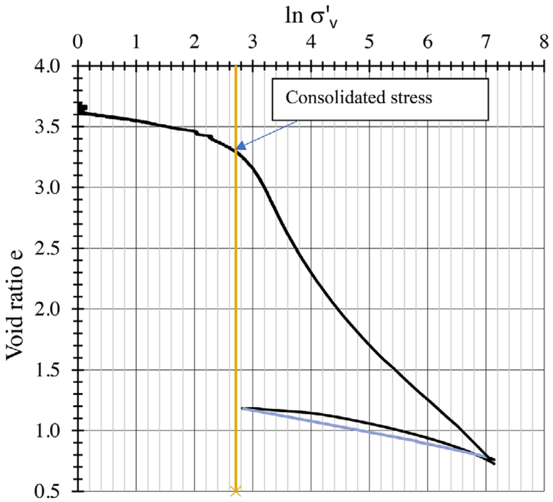

(A) Soil sample 1:2.60 to 2.62m

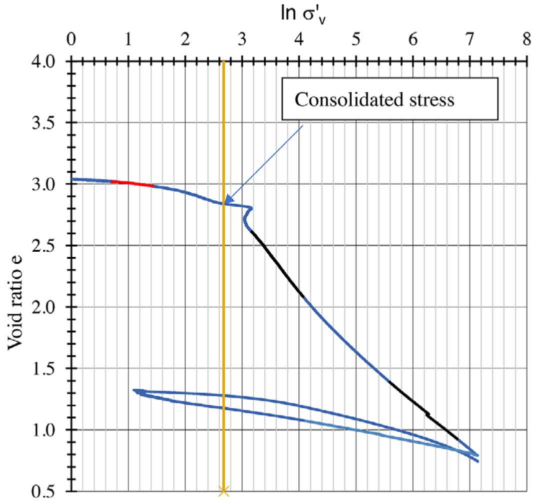

(B) Soil sample 2:3.98 to 4.00 m

FIGURE B2 | $e - \ln \sigma'_v$ Curves from CRS oedometer Tests: (A) Soil Sample 1 and (B) Soil Sample 2.

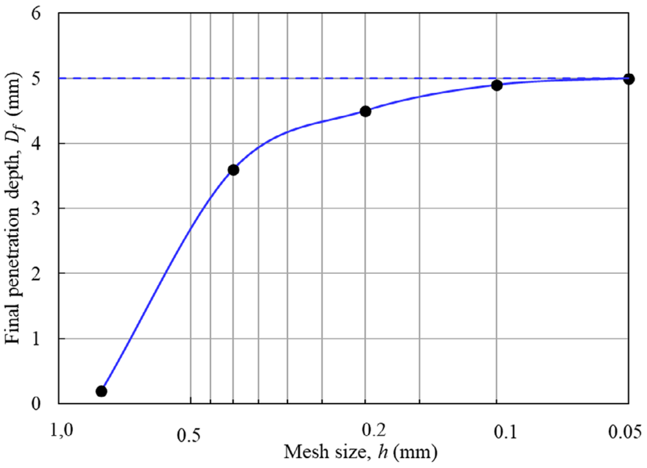

(A) Drop height = 0 mm

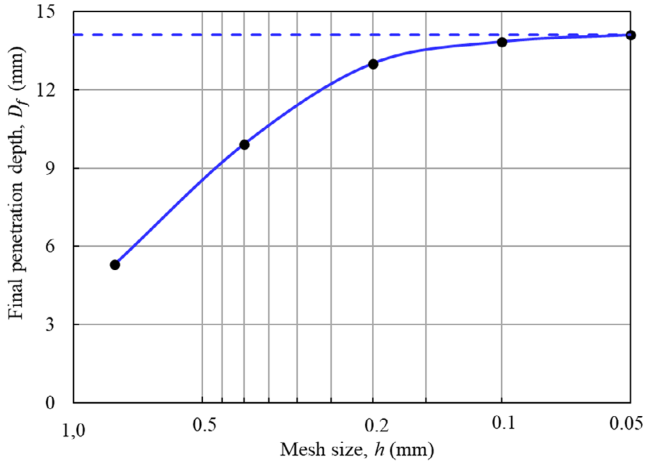

(B) Drop height = 20mm

FIGURE C1 | Influence of spatial discretization on the penetration depth of FFCP.

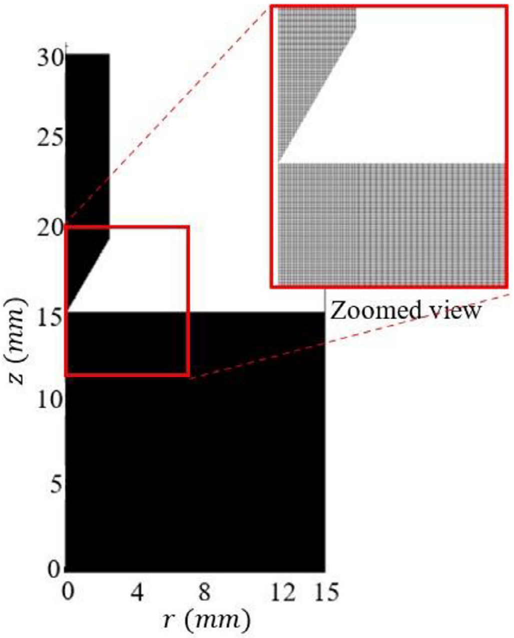

FIGURE C3 | Discretized soil domain used in the numerical analysis for D_h= 0 mm.

that with an increase in the number of grid cells, the numerical value of the final penetration depth of the FFCP increases. The final penetration depth does not change significantly for h <0.1 mm. Therefore, the present analysis uses h = 0.1 mm for the present numerical simulation. Figure C1 illustrates the high sensitivity of the numerical simulation to grid density. Figure C2 displays displacement contours corresponding to different grid densities for FFCPT numerical simulation. The FFCP-soil interaction is insufficiently accurate with a lower grid density, leading to qualitatively different results. The development of displacement in soil during the FFCP penetration process associated with different grid densities are presented in video files (Dh0-MS0.8.mpg to Dh20-MS0.05.mpg) in the supplementary material. Figure C3 shows the discretized soil domain used in the numerical analysis for D_h= 0 mm and zoomed view near FFCP-Soil contact.

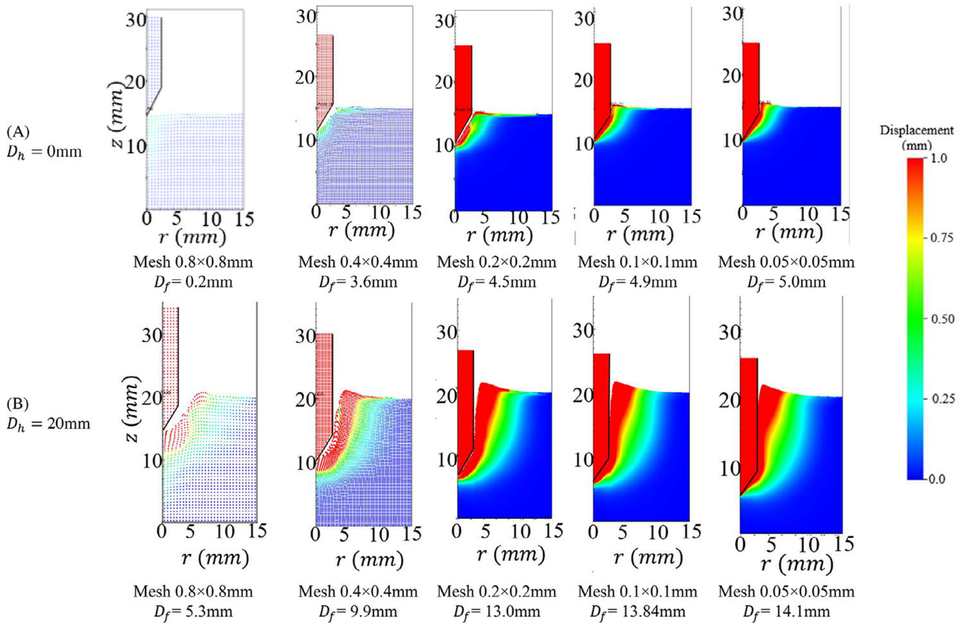

FIGURE C2 | Penetration depth of different mesh densities. (Refer to supplementary material Dh0-MS0.8.mpg to Dh20-MS0.05.mpg).